

Petrology of Sedimentary Rocks

G421P13, summer semester, 2/1 hours, 3-4th year

4. Evaporites, cherts, ironstones, phosphates

Karel Martínek

Institute of Geology and Palaeontology

Evaporites

sea water chemistry, mineral succession of isothermic evaporation of sea water

typical sedimentary environment: subaqueatic, subaerial - sabcha, shelf margin - lagoon, salina, isolated basin, playa

microstructures gypsum-anhydrite, halite, lacustrine evaporites

lateral and vertical distribution of facies driven by relative sea water level changes

diapirism

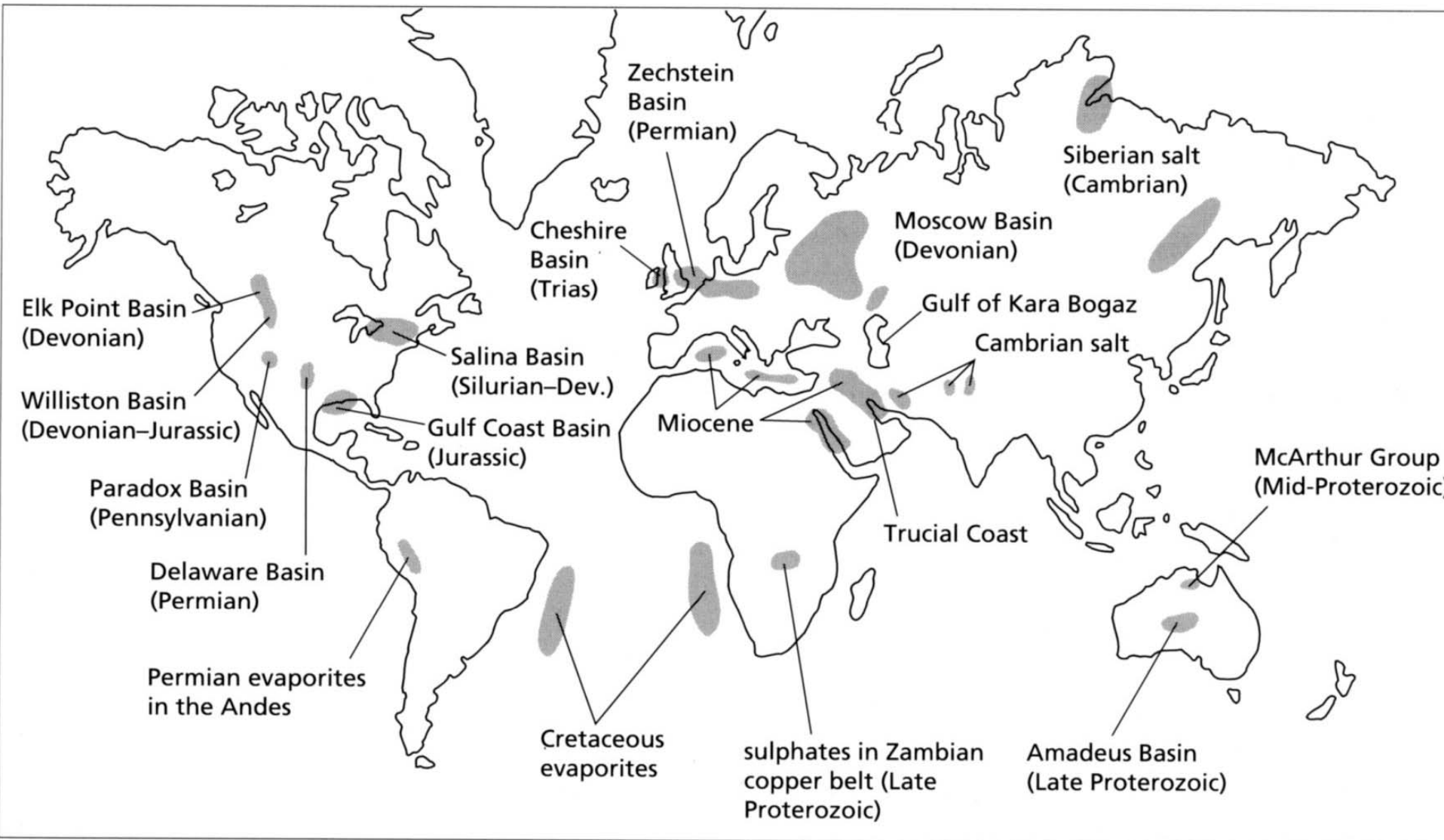


Table 5.1 The common marine and non-marine evaporite minerals

| Marine evaporite minerals | | Non-marine evaporite minerals | |
|---------------------------|--------------------------------------------------------------------------------------|-------------------------------|--------------------------------------------------------------------------|
| halite | NaCl | halite, gypsum, anhydrite | |
| sylvite | KCl | epsomite | MgSO ₄ · 7H ₂ O |
| carnallite | KMgCl ₃ · 6H ₂ O | trona | Na ₂ CO ₃ · NaHCO ₃ · 2H ₂ O |
| kainite | KMgClSO ₄ · 3H ₂ O | mirabilite | Na ₂ SO ₄ · 10H ₂ O |
| anhydrite | CaSO ₄ | thenardite | NaSO ₄ |
| gypsum | CaSO ₄ · 2H ₂ O | bloedite | Na ₂ SO ₄ · MgSO ₄ · 4H ₂ O |
| polyhalite | K ₂ MgCa ₂ (SO ₄) ₄ · 2H ₂ O | gaylussite | Na ₂ CO ₃ · CaCO ₃ · 5H ₂ O |
| kieserite | MgSO ₄ · H ₂ O | glauberite | CaSO ₄ · Na ₂ SO ₄ |

Table 5.2 The composition of sea water expressed in parts per million and percentage of total dissolved species. For comparison, the composition of world average river water, with a salinity of around 120 ppm is also given. Data from Krauskopf (1979)

| Dissolved species | Seawater | | River water |
|---------------------------------|----------|------------|-------------|
| | ppm | % of total | |
| Cl ⁻ | 18 000 | 55.05 | 7.8 |
| Na ⁺ | 10 770 | 30.61 | 6.3 |
| SO ₄ ²⁻ | 2715 | 7.68 | 11.2 |
| Mg ²⁺ | 1290 | 3.69 | 4.1 |
| Ca ²⁺ | 412 | 1.16 | 15.0 |
| K ⁺ | 380 | 1.10 | 2.3 |
| HCO ₃ ⁻ | 140 | 0.41 | 58.4 |
| Br ⁻ | 67 | 0.19 | 0.02 |
| H ₃ BO ₃ | 26 | 0.07 | 0.1 |
| Sr ²⁺ | 8 | 0.03 | 0.09 |
| F ⁻ | 1.3 | 0.005 | 0.09 |
| H ₄ SiO ₄ | 1 | 0.004 | 13.1 |

four main stages of salt precipitation during isothermic sea water evaporation

Tab. 19

Čtyři základní stádia krystalizace solí při izotermickém odpařování mořské vody

| stádium | hlavní produkt krystalizace | násobek koncentrace rozpuštěných látek | snížení objemu solanky |
|---------|-----------------------------------------------------------------|----------------------------------------|------------------------|
| I. | karbonáty Ca | 1 - 3,35 | 0 - 1/5 |
| II. | sulfáty (hlavně sádrovec a anhydrit) | 3,35 - 10,96 | 1/5 - 1/10 |
| III. | chloridy Na (hlavně helit + zbytkové sulfáty) | 10,96 - 60,43 | 1/10 - 1/20 |
| IV. | chloridy a sulfáty K a Mg (+ malé množství halitu a Ca sulfátu) | nad 60,43 | nad 1/20 |

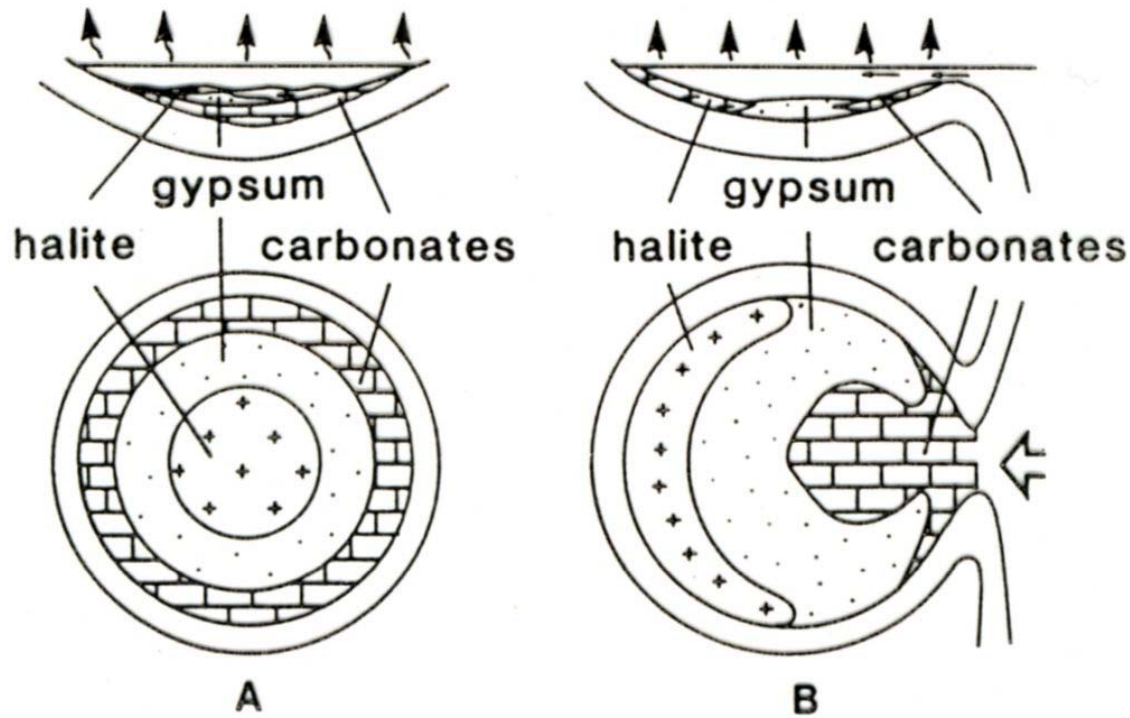
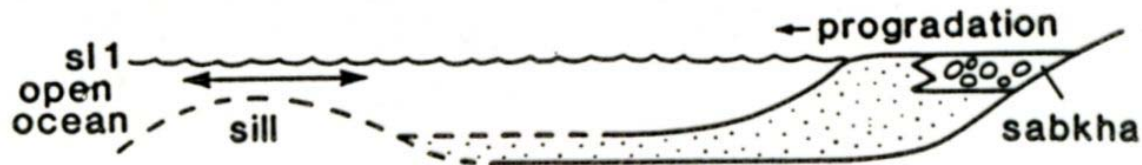
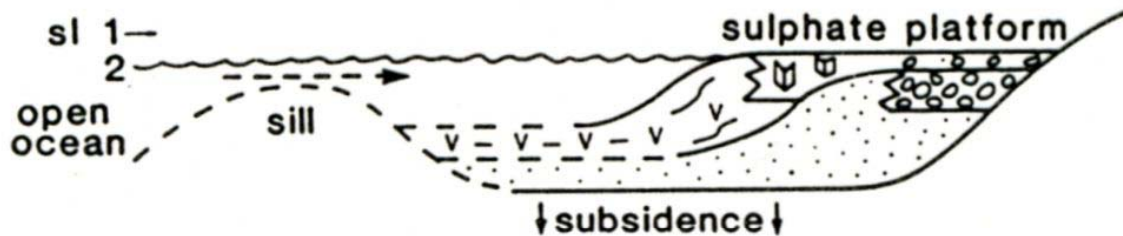


Fig. 5.20 Broad patterns of evaporite facies. A, Bullseye pattern, with the most soluble salts in the basin centre, typical of completely enclosed basins. B, Tear-drop pattern, typical of restricted basins with near-permanent connection to the open ocean, where the most soluble salts occur farthest away from the basin entrance. After Schmaltz (1969).

A high sea-level: normal marine, carbonate deposition



B intermediate sea-level: restricted marine, gypsum deposition



C low sea-level: salt lake-saline pan, halite precipitation

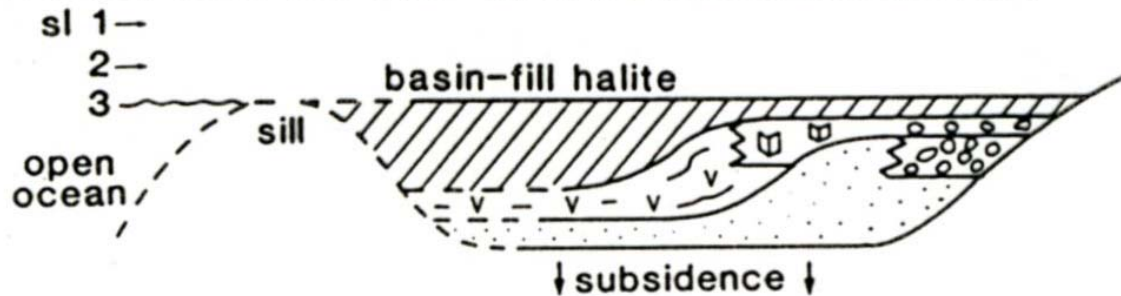


Fig. 5.21 Model for evaporite deposition in an intracratonic basin, where eustatic sea-level changes are a major control. After Clark & Tallbacka (1980).

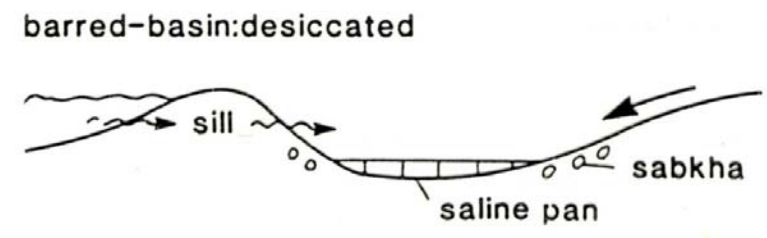
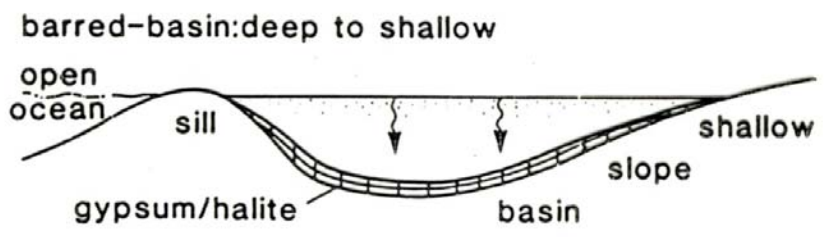
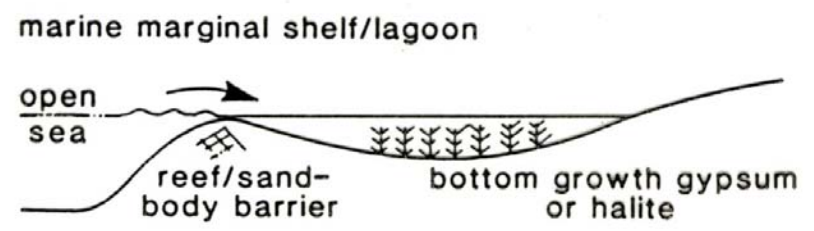
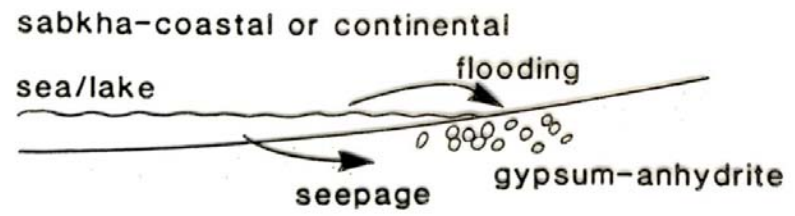
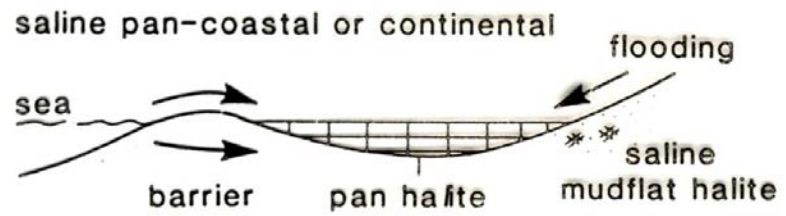


Fig. 5.2 Principal depositional environments of evaporites.

Table 5.3 The theoretical thickness of salts precipitated from sea water compared with the thickness of these salts in the Permian Zechstein of Germany, expressed as 100 m of precipitated evaporite. Note that there is much more CaSO₄ and much less Mg and K salts in the Zechstein deposits compared with the theoretical. Also shown is the approximate thickness of the various salts produced by the evaporation of a column of sea water 1000 m high. After Borchert & Muir (1964)

| Component | Mineral | Thickness in 100 m of evaporite | | Salt thickness from 1000 m of sea water |
|-------------------------------------|------------------------------|---------------------------------|-------------------|-----------------------------------------|
| | | from sea water | Permian Zechstein | |
| MgCl ₂ | in bischofite and carnallite | 9.4 | 0.5 | 1.5 |
| KCl | sylvite and in carnallite | 2.6 | 1.5 | 0.4 |
| MgSO ₄ | in kieserite | 5.7 | 1.0 | 1.0 |
| NaCl | halite | 78 | 78 | 12.9 |
| CaSO ₄ | anhydrite | 3.6 | 16 | 0.6 |
| CaCO ₃ | calcite | 0.4 | 3 | 0.1 |
| CaMg(CO ₃) ₂ | dolomite | | | |

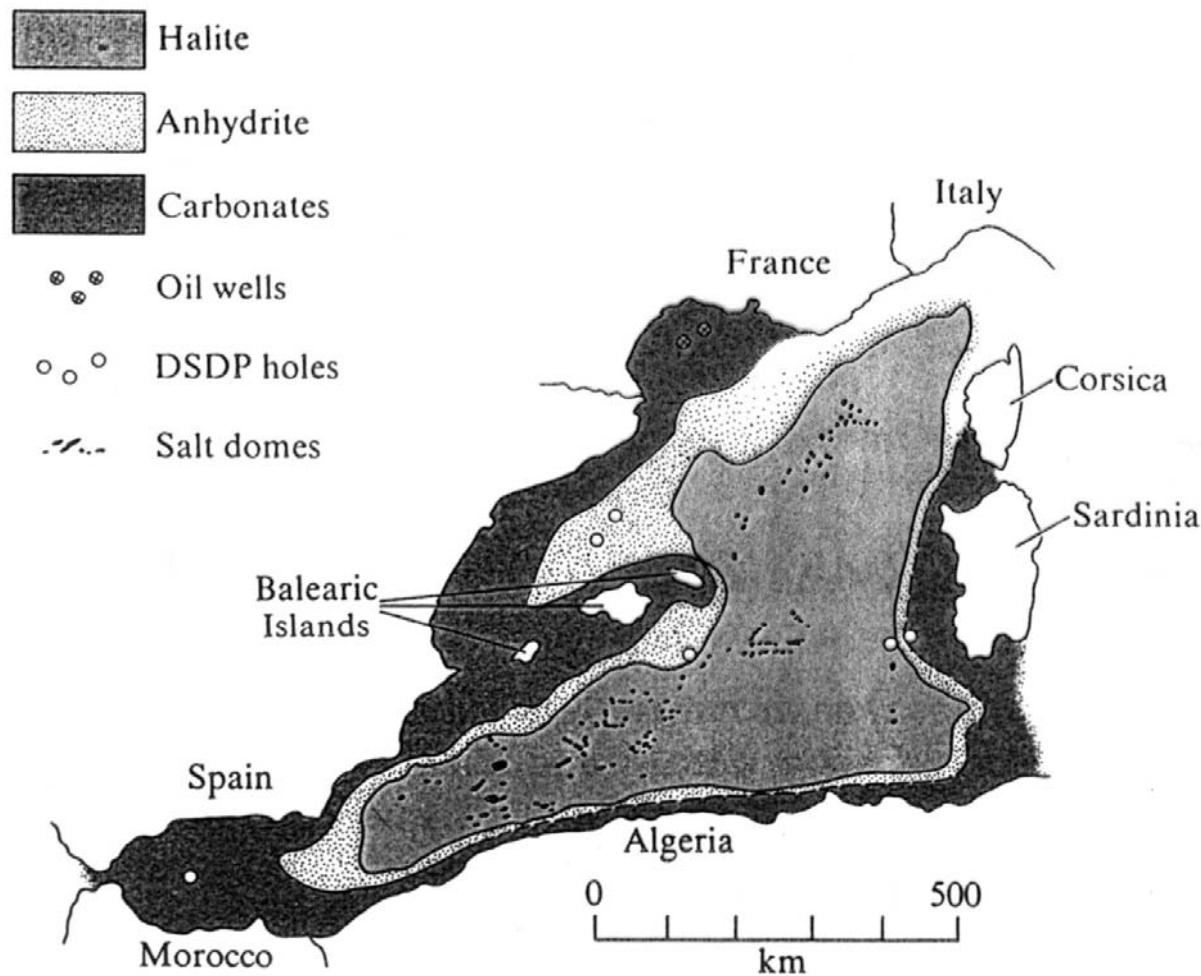


Figure 10-21

Evaporite distribution in Miocene rocks of Balearic Basin of Mediterranean Sea immediately east of Strait of Gibraltar. Balearic was one of several topographically low salt pans on floor of desiccated Mediterranean. Potash salts (not shown) occur in middle of halite area. [Hsü, 1972, *Earth-Science Rev.*, 8, p. 390.]

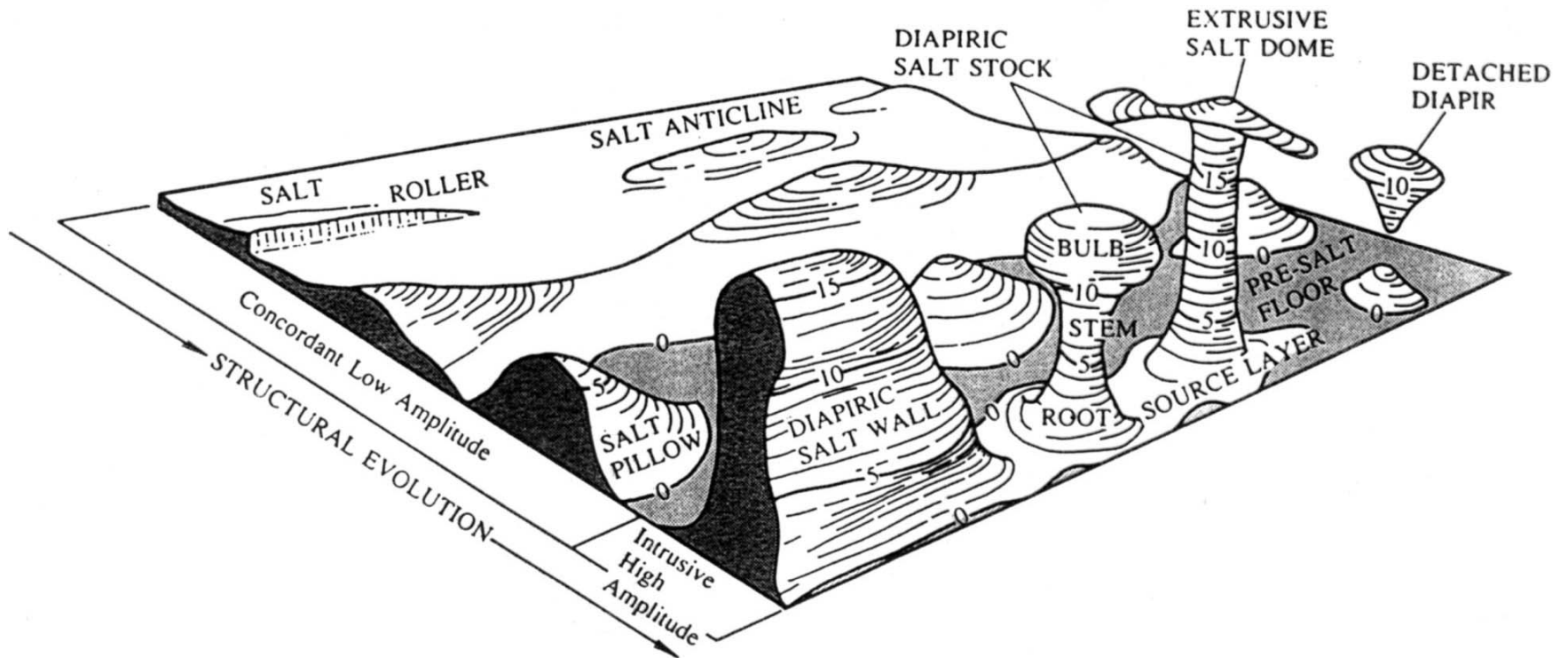


Figure 10-11

The main configurations of salt structures. Structure contours are in arbitrary units. Larger features such as salt nappes cannot be shown at this scale. [Jackson and Talbot, 1986, p. 306.]

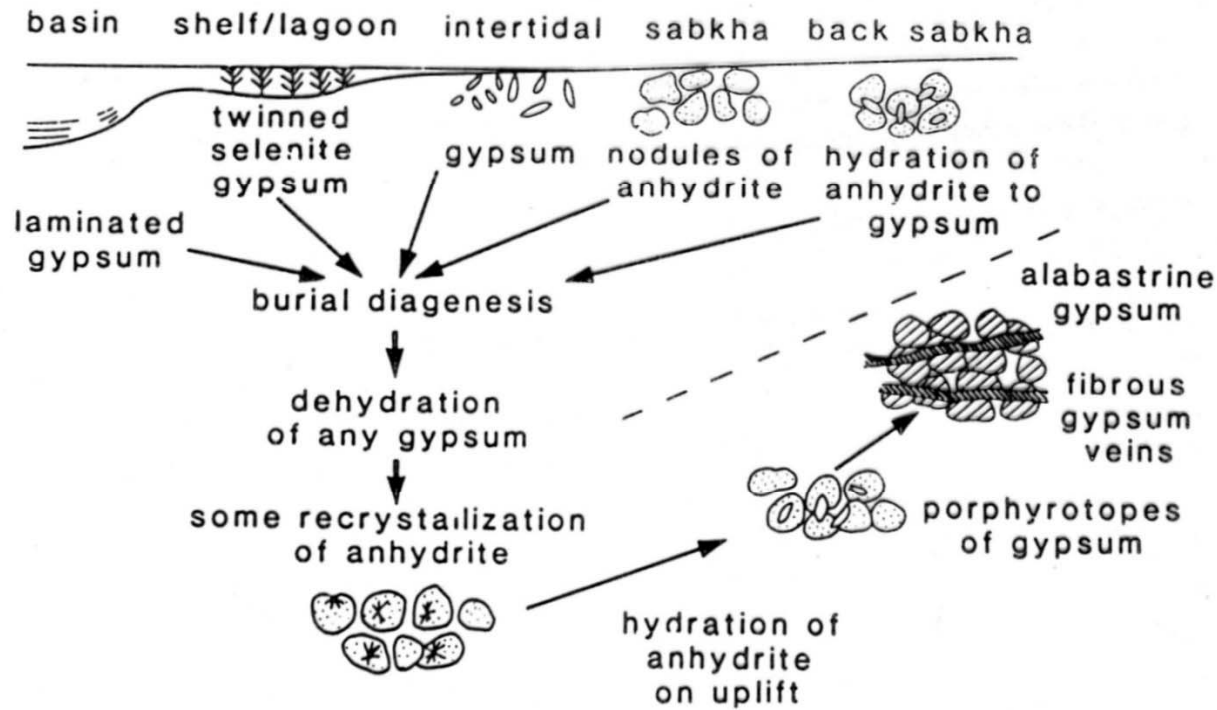


Fig. 5.3 The 'gypsum-anhydrite cycle' showing mineral and textural changes from the surface, into the subsurface and on uplift.

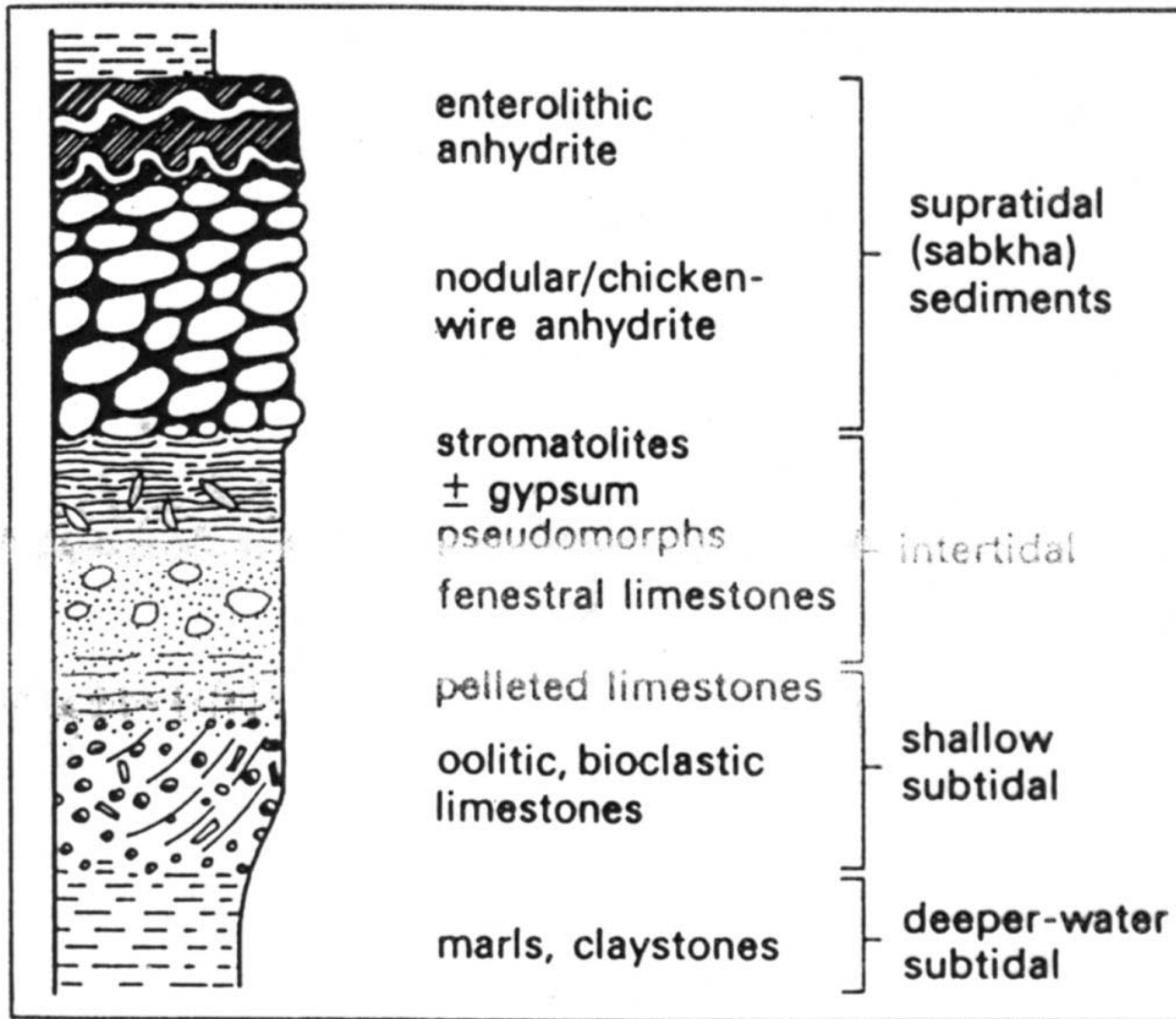


Fig. 5.17 A sabkha cycle. Such cycles typically range from several to several tens of metres in thickness.

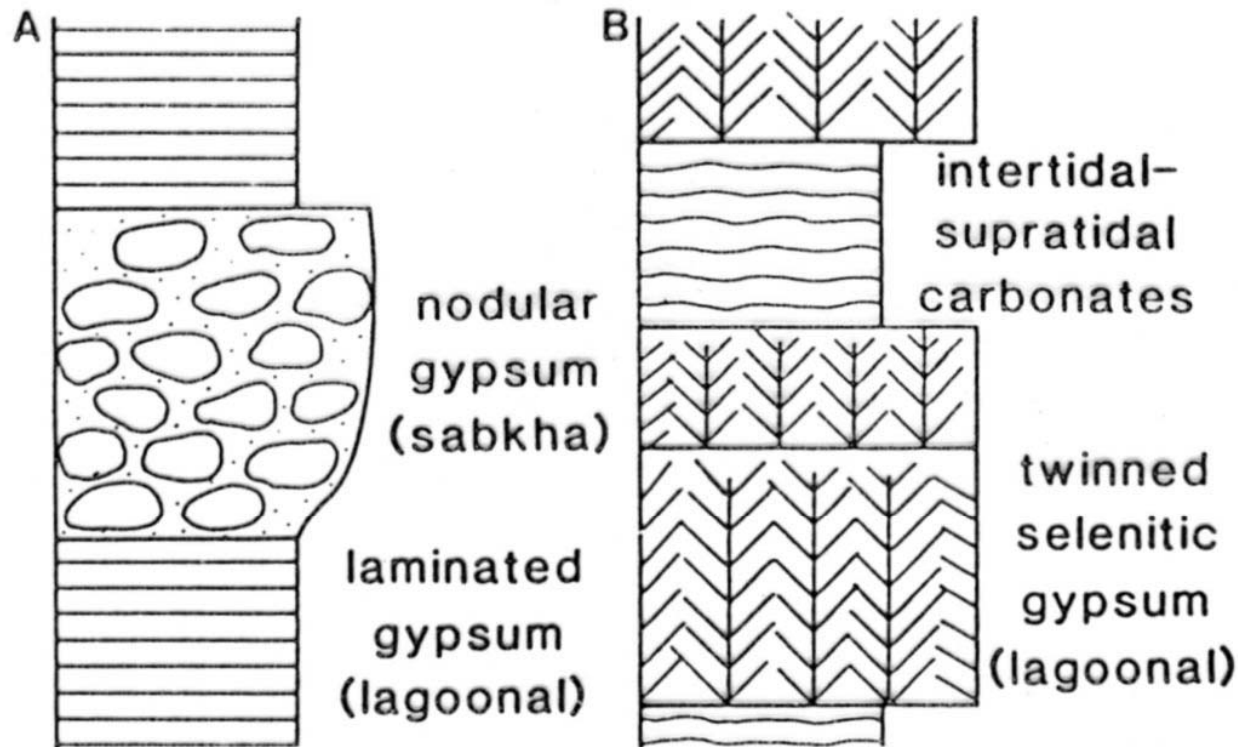


Fig. 5.18 Two less common types of evaporite cycle. A, Laminated gypsum passing up into nodular gypsum. B, Lagoonal, selenitic gypsum passing up into intertidal-supratidal carbonates.

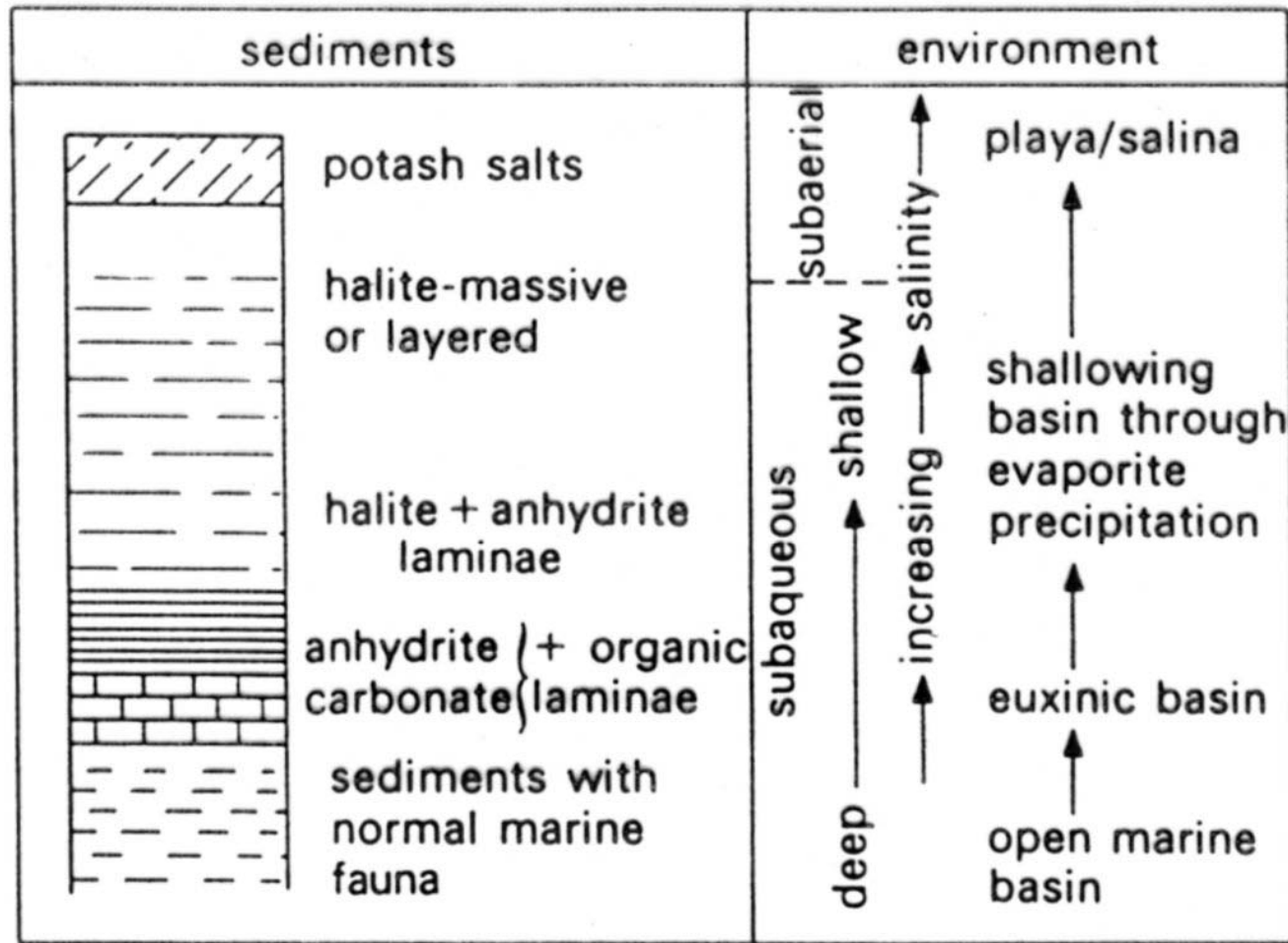


Fig. 5.19 Evaporite sequence formed in an initially deep, marine barred-basin, with periodic replenishment.

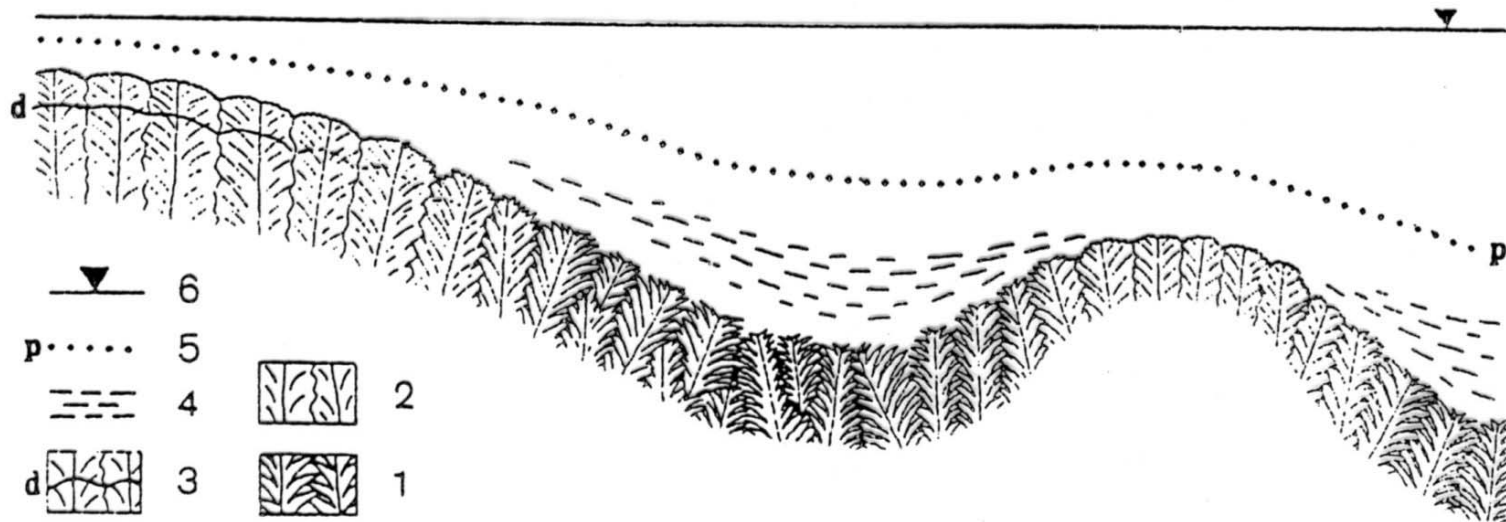


Fig. 7 Model środowiska sedimentacji gipsów szklicowych o budowie palisadowej (subfacje 2a i 2b)
 1 - kryształy o budowie szkieletowej (subfacja 2a), 2 - kryształy o budowie masywnej (subfacja 2b), 3 -
 powierzchnie rozpuszczania (d), 4 - zawieszina ilasta, 5 - pyknoklina (p), 6 - poziom wody

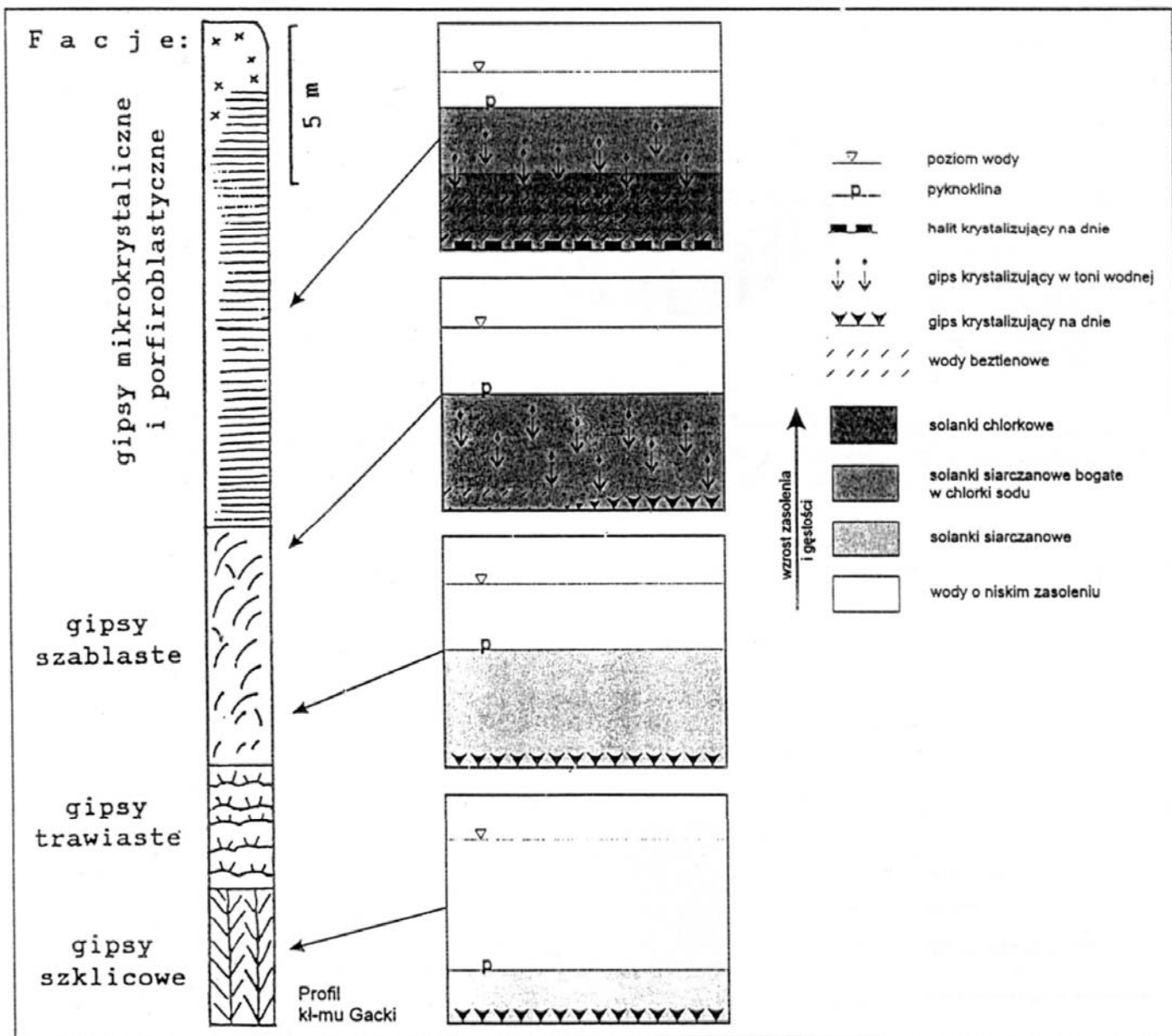


Fig. 27 Ewolucja składu i struktury wód basenu ewaporacyjnego

lacustrine evaporites

Table 5.4 The water chemistry of five salt lakes (in ppm). The main point to note is the great variability in the relative concentrations of the constituents between lakes

| | Dead Sea | Great Salt Lake, Utah | Mono Lake, California | Borax Lake, California | Gulf of Kara, Bogaz, USSR |
|-------------------------------|----------|-----------------------|-----------------------|------------------------|---------------------------|
| Cl ⁻ | 208 020 | 112 900 | 15 100 | 5945 | 142 500 |
| SO ₄ ²⁻ | 540 | 13 590 | 7530 | 22 | 46 900 |
| HCO ₃ ⁻ | 240 | 180 | 26 430 | 6668 | — |
| Na ⁺ | 34 940 | 67 500 | 21 400 | 6199 | 81 200 |
| K ⁺ | 7560 | 3380 | 1120 | 322 | |
| Ca ²⁺ | 15 800 | 330 | 11 | nil | 4900 |
| Mg ²⁺ | 41 960 | 5620 | 32 | 30.7 | 19 900 |
| Total salinity | 315 040 | 203 490 | 71 900 | >19 400 | >293 000 |

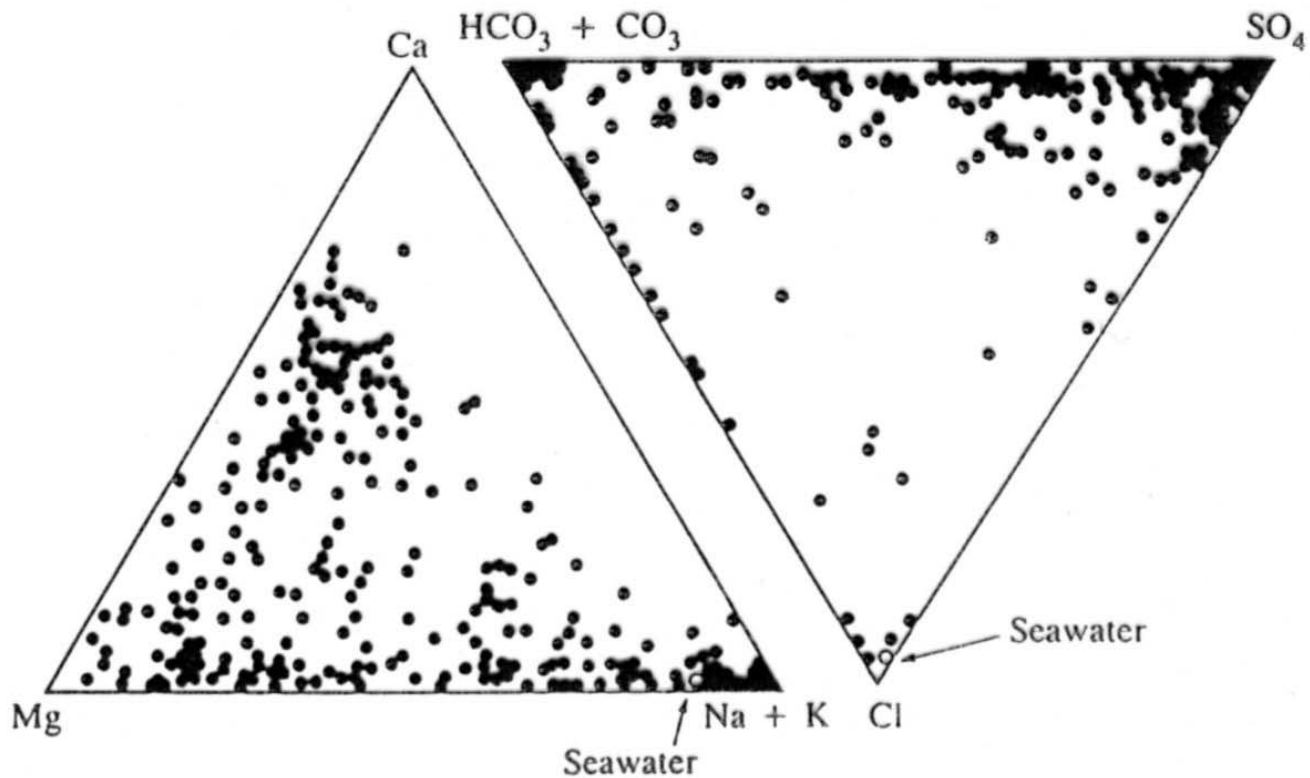
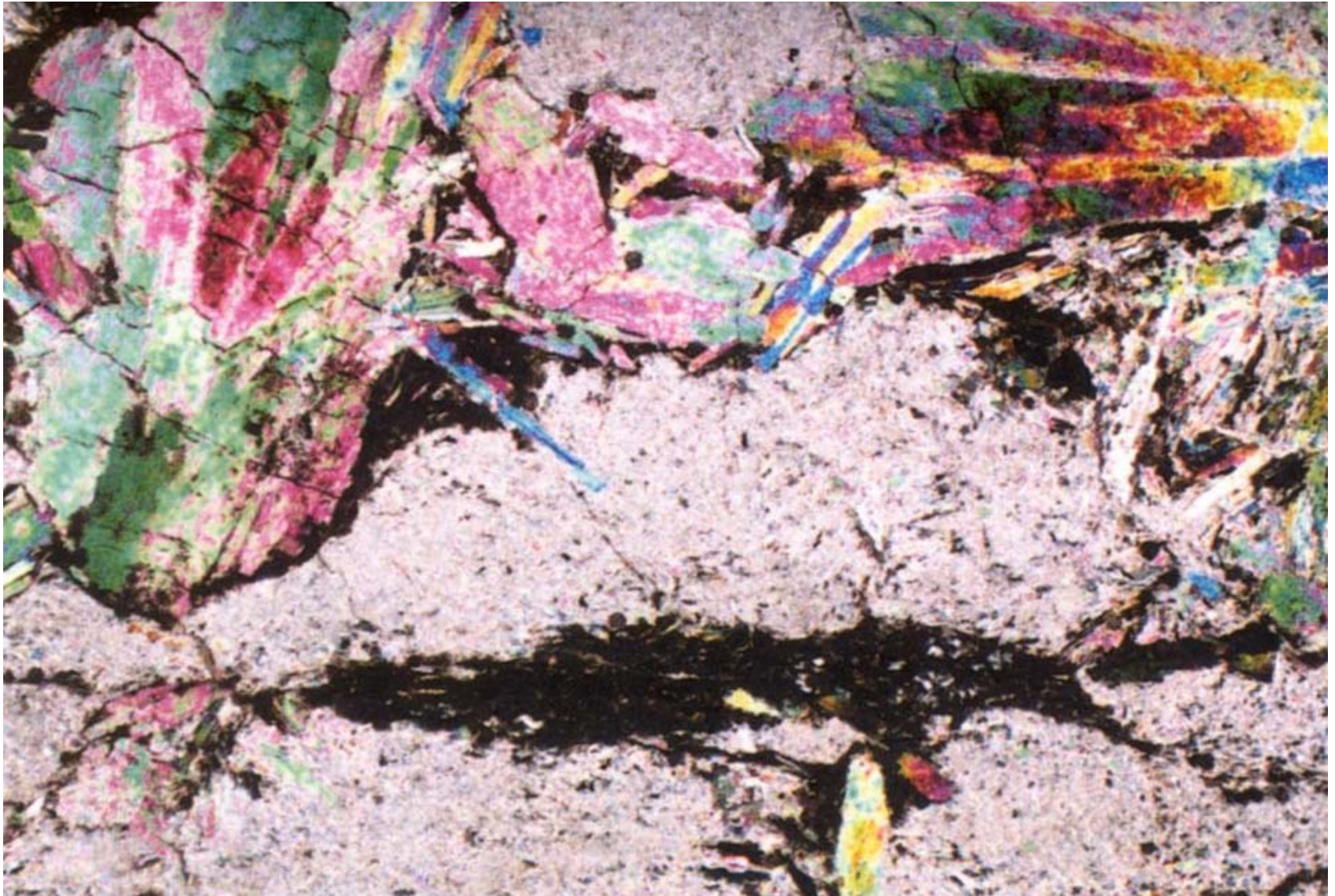


Figure 10-3

This triangular diagram with standard elemental poles displays water compositions for 379 saline lakes in western Canada. Also shown is the location of seawater in each triangle. It is evident that many of these waters show little or no influence of marine water. [Last, 1989, *Sedimentary Geol.*, 64, 209.]

anhydrite (large crystals and laths, high bir. colours) and microcrystalline gypsum nodules (low bir. colours)



anhydrite (large prismatic crystals, high bir. colours) and microcrystalline gypsum nodules (low bir. colours)



Cherts

mineralogy - opal A, opal CT, quartz

microstructures - euhedral, microquartz, megaquartz, chalcedonic quartz

sources, solubility

sed. environments – marine, lacustrine (alkaline lakes), spring cherts

diagenesis, silicification

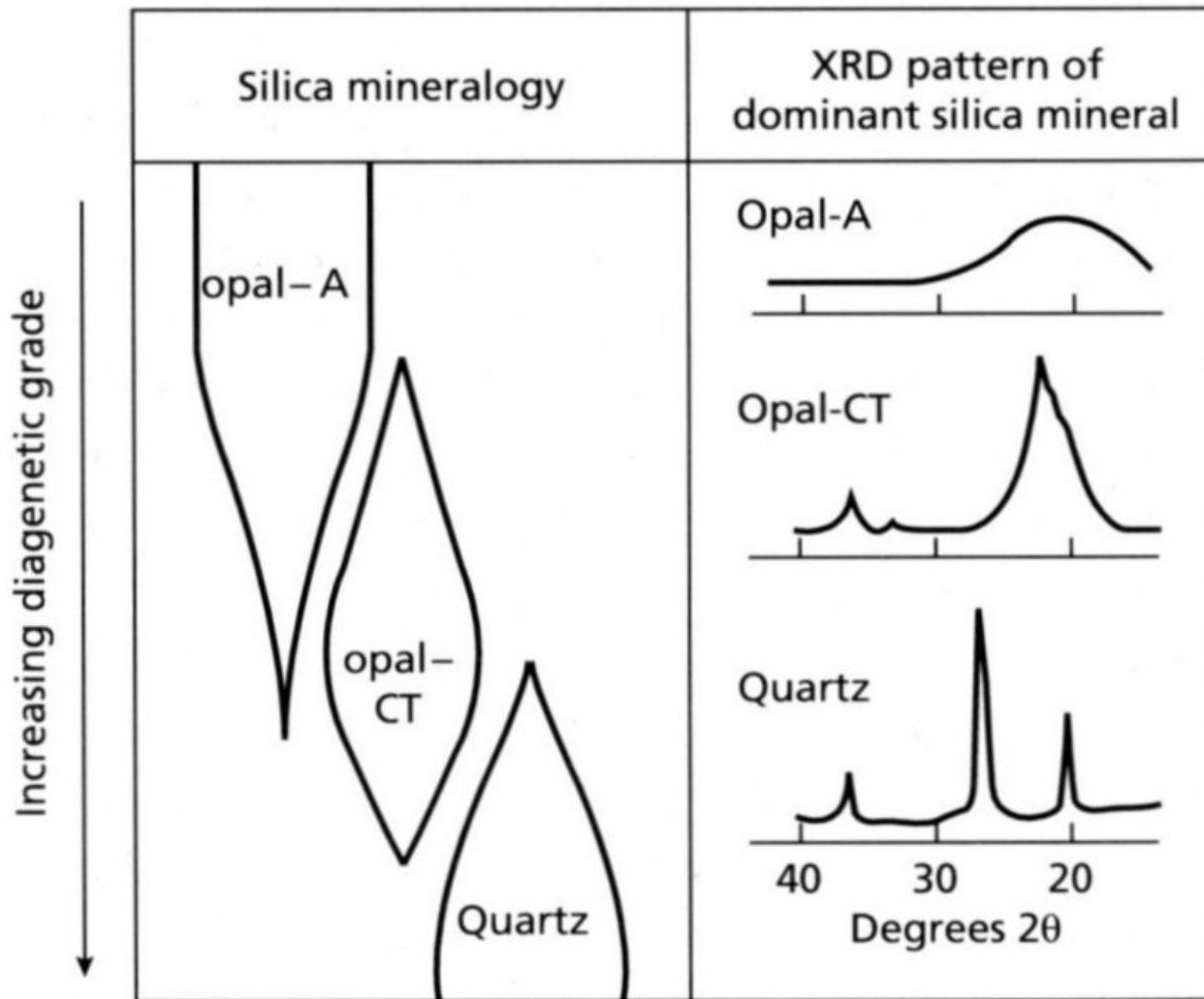
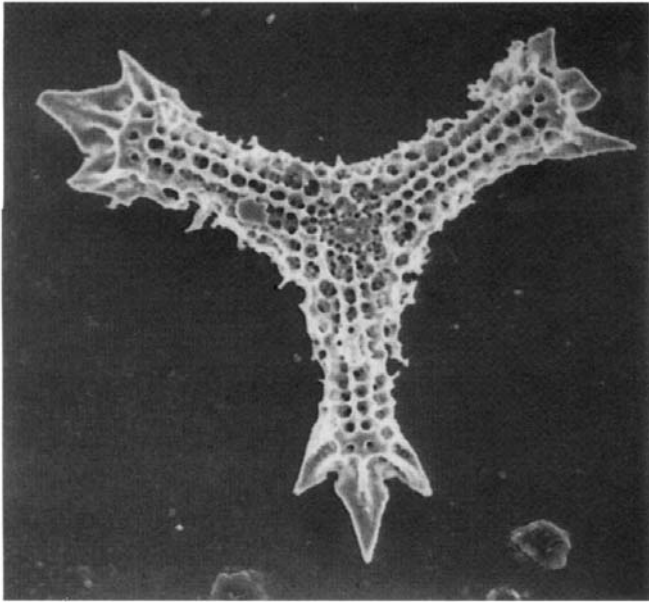
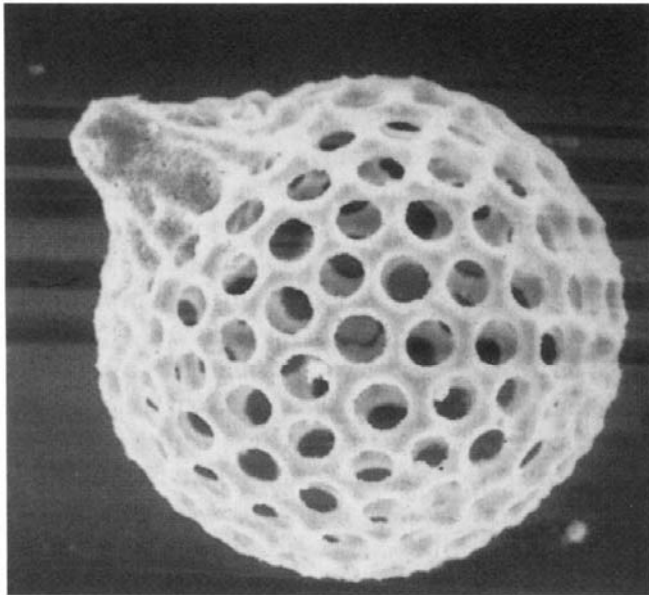
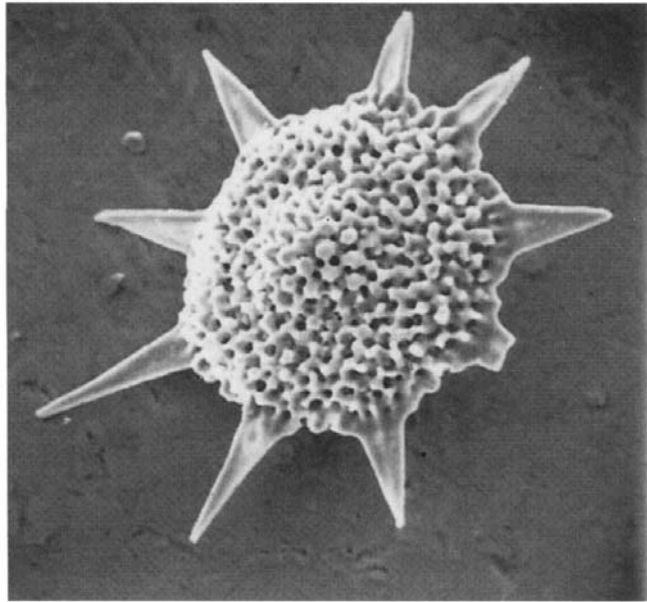


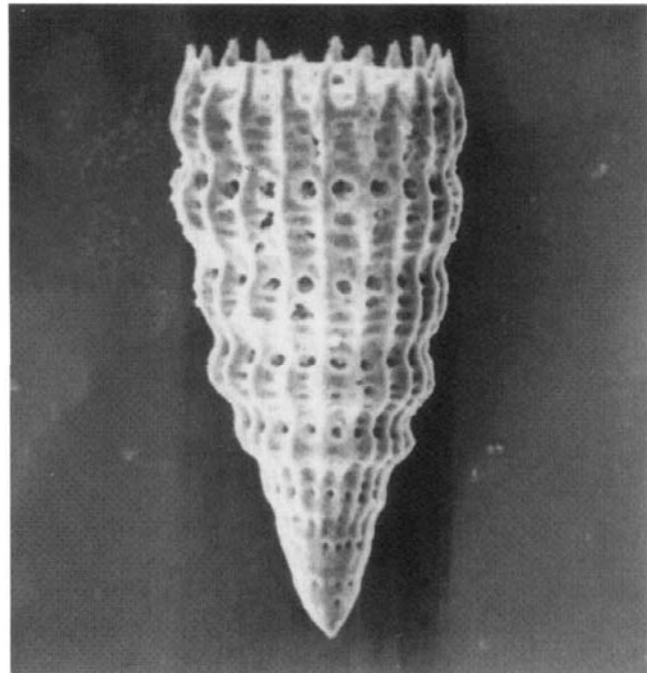
Fig. 9.6 Schematic changes in silica mineralogy with increasing diagenesis, and X-ray diffraction patterns for opal-A, opal-CT and quartz showing the increasing crystallinity. After Pisciotta (1981).



(a)



(c)



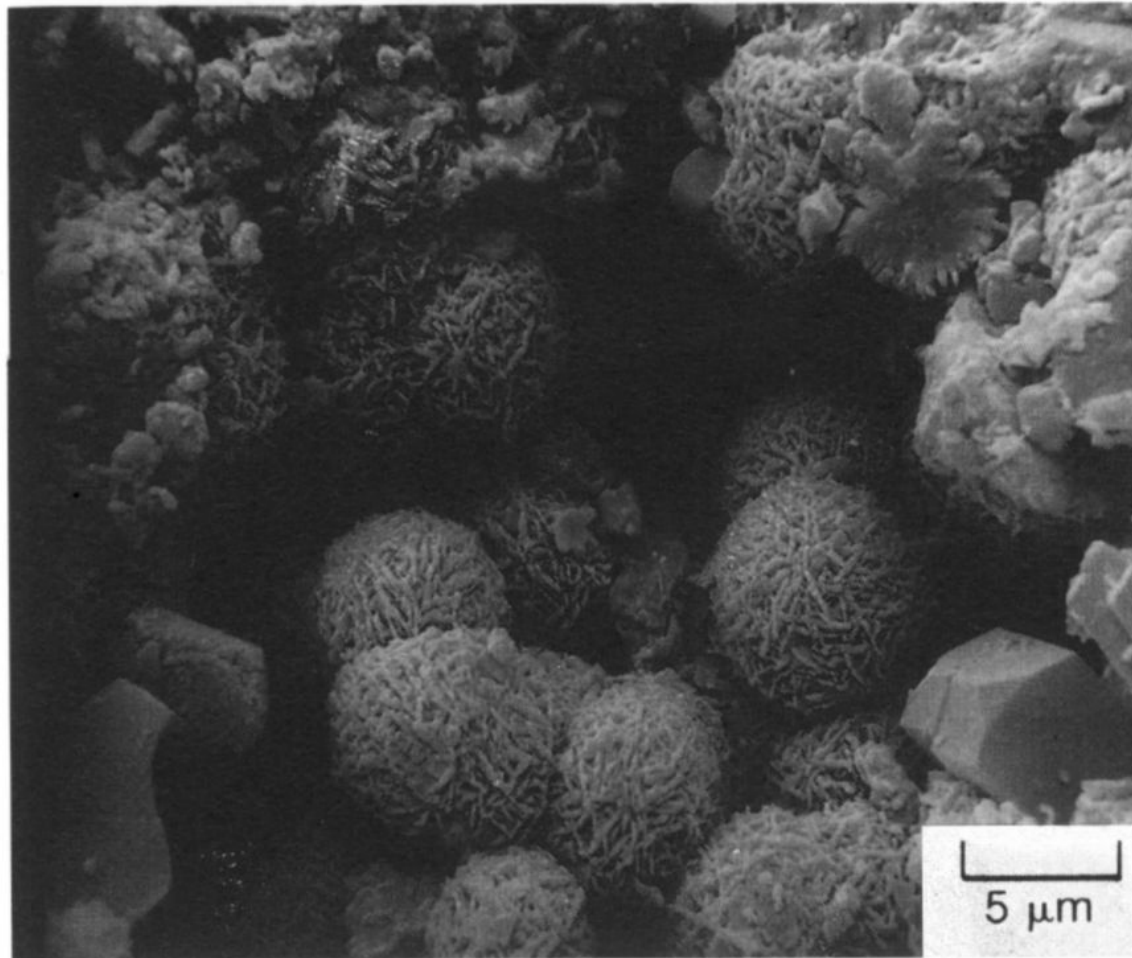


Fig. 9.7 Lepispheres of opal-CT growing in voids in silicified Eocene chalk from the Arabian Sea. Sample from 630 m below sea floor. Prismatic crystals are clinoptilolite (a zeolite). Scanning electron micrograph.

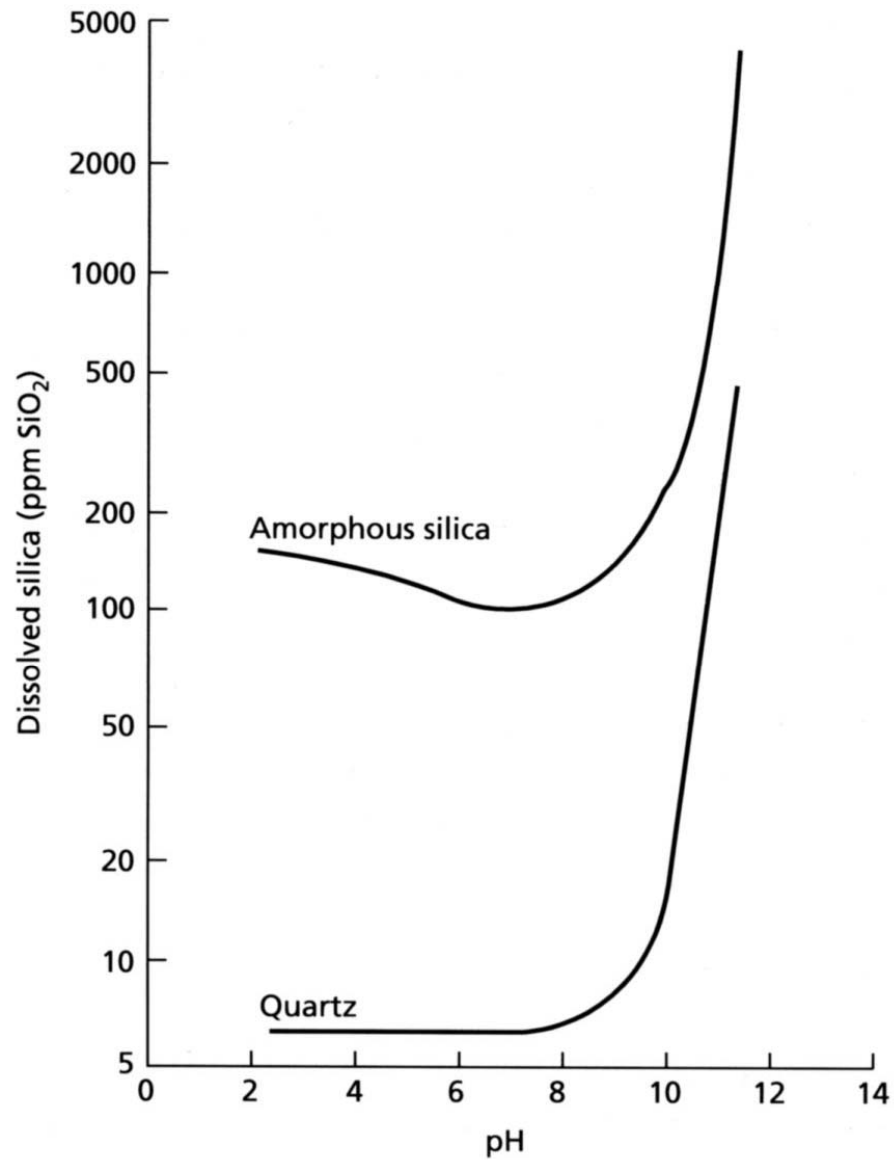
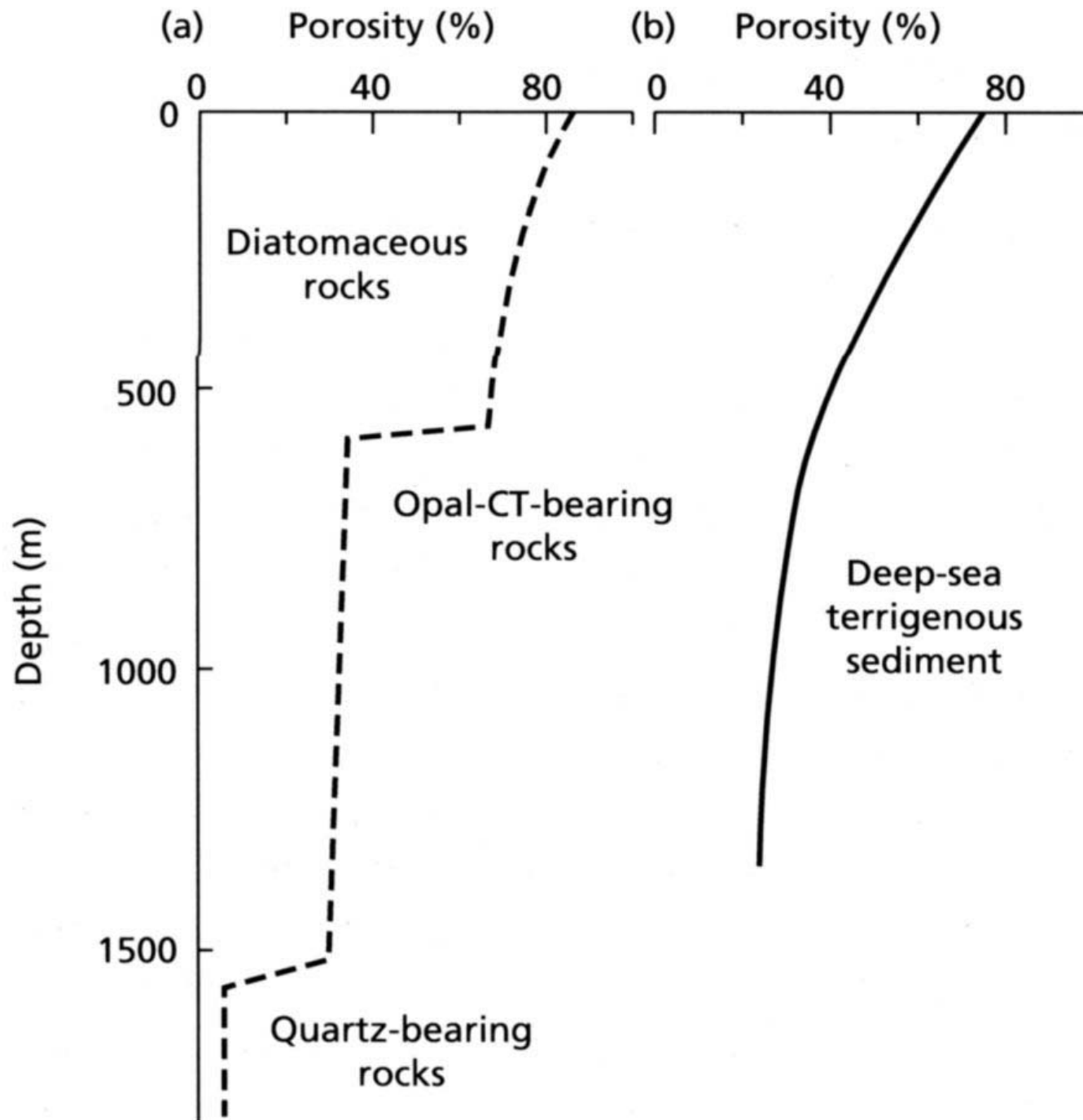


Fig. 9.8 The solubility of quartz and amorphous silica at 25 °C. At pH values less than 9, the silica is in solution as undissolved orthosilicic acid (H_4SiO_4); above pH 9, this dissociates into $\text{H}_3\text{SiO}_4^{2-}$ and $\text{H}_2\text{SiO}_4^{2-}$.



Ironstones

sources & transport Fe, eH-pH stability field Fe ox.-hox.

early diagenesis

glaukony

granular facies, impregnation, coatings; authigenic Fe glaukonitic smectite, early diag. Fe, K glaukonitic mica; driving mechanisms: abundance of Fe, K, balance between clastic input and washing, low sedimentation rate ($10^3 - 10^6$ let)

ferromanganese nodules

Table 6.1 The iron minerals of sedimentary rocks

| | |
|-----------|---------------------------------------------------------------------------------------------------|
| Oxides | hematite $\alpha\text{-Fe}_2\text{O}_3$ |
| | magnetite Fe_3O_4 |
| | goethite $\alpha\text{-FeO}\cdot\text{OH}$ |
| | limonite $\text{FeO}\cdot\text{OH}\cdot n\text{H}_2\text{O}$ |
| Carbonate | siderite FeCO_3 |
| Silicates | berthierine $(\text{Fe}_4^{2+} \text{Al}_2) (\text{Si}_2\text{Al}_2) \text{O}_{10} (\text{OH})_8$ |
| | chamosite $(\text{Fe}_5^{2+} \text{Al}) (\text{Si}_3\text{Al}) \text{O}_{10} (\text{OH})_8$ |
| | greenalite $\text{Fe}_6^{2+} \text{Si}_4 \text{O}_{10} (\text{OH})_8$ |
| | glauconite $\text{KMg}(\text{FeAl}) (\text{SiO}_3)_6\cdot 3\text{H}_2\text{O}$ |
| Sulphides | pyrite FeS_2 |
| | marcasite FeS_2 |

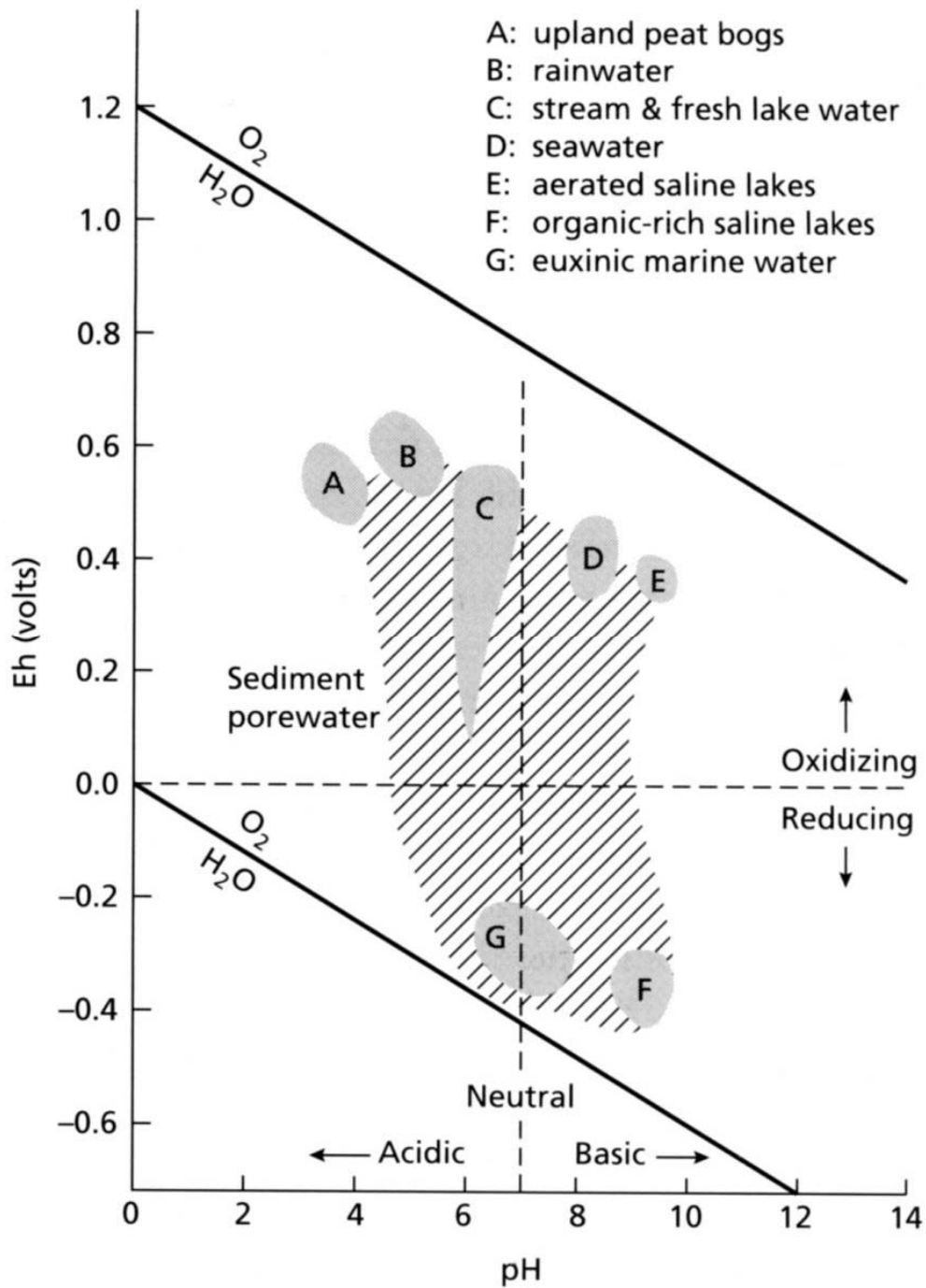
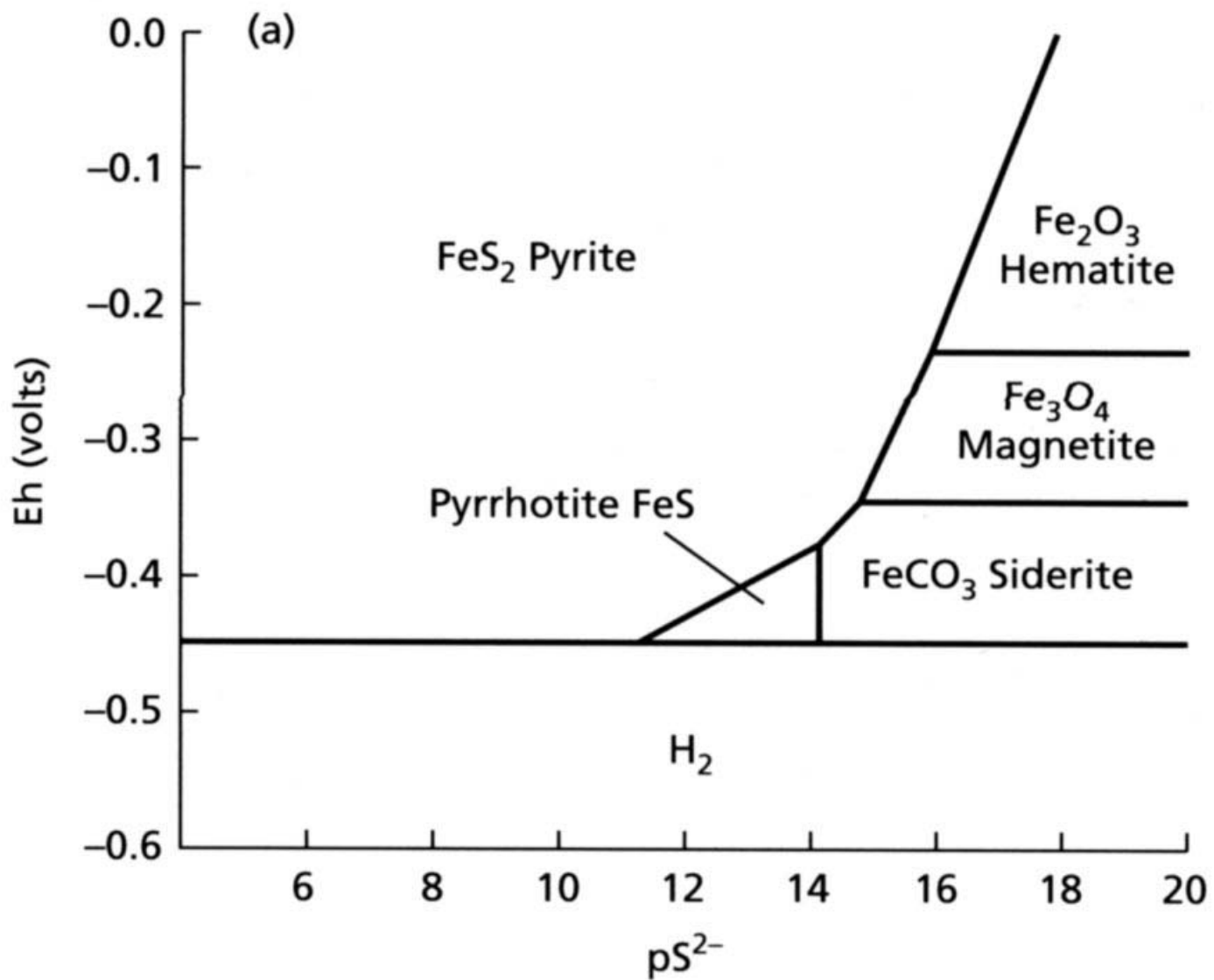


Table 6.2 Geochemical classification of early diagenetic environments and the characteristic phases present. After Berner (1981)

| Environment | Characteristic phases |
|------------------------|---------------------------------------------------------------------------------------------------------------|
| <i>Oxic</i> | hematite, goethite, MnO ₂ -type minerals, no organic matter |
| <i>Anoxic</i> | |
| 1 sulphidic | pyrite, marcasite, rhodochrosite, organic matter |
| 2 non-sulphidic | |
| (a) post-oxic | glauconite, berthierine, no sulphide minerals, minor organic matter (also siderite, vivianite, rhodochrosite) |
| (b) methanic | siderite, vivianite, rhodochrosite, earlier formed sulphide minerals, organic matter |



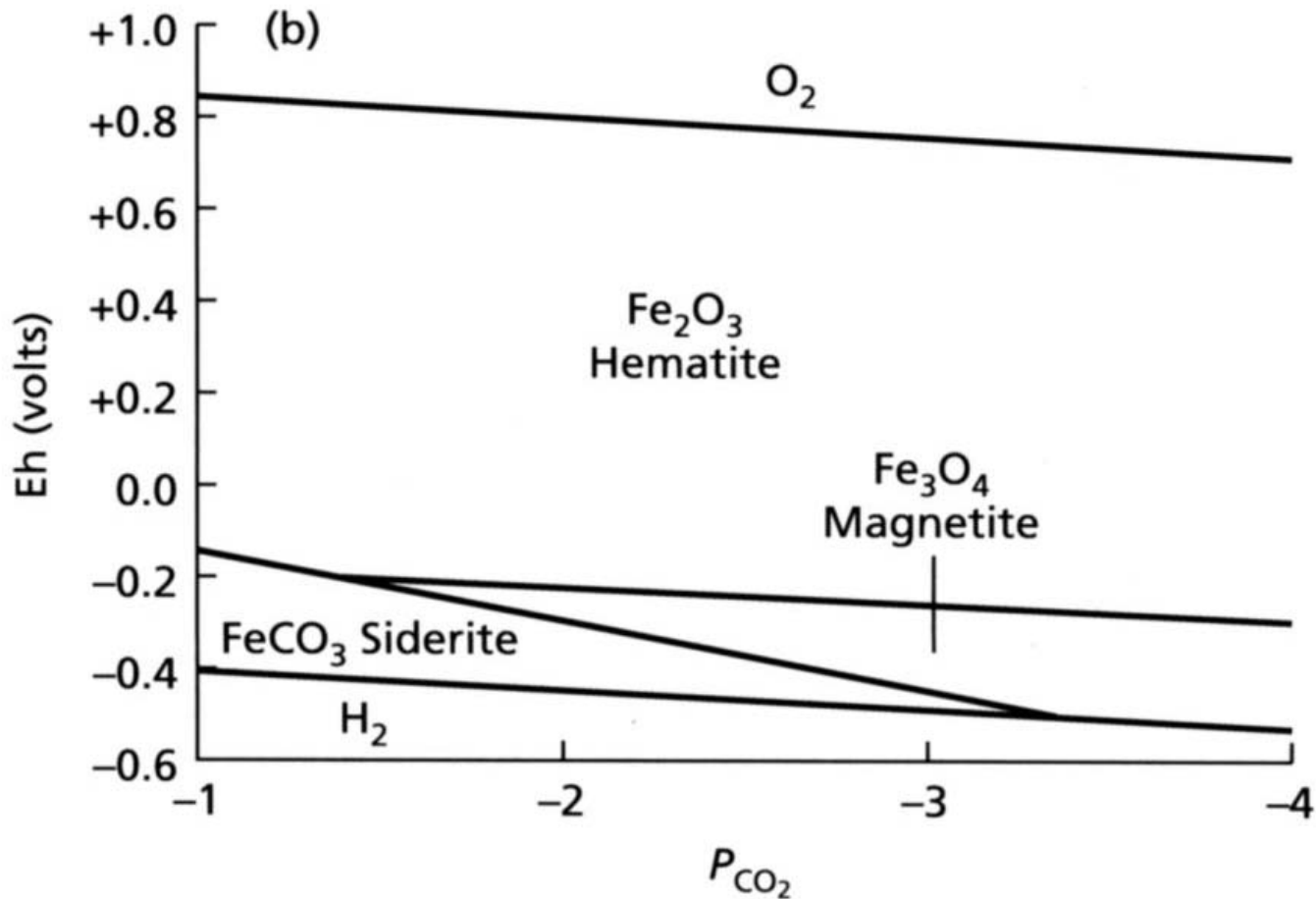
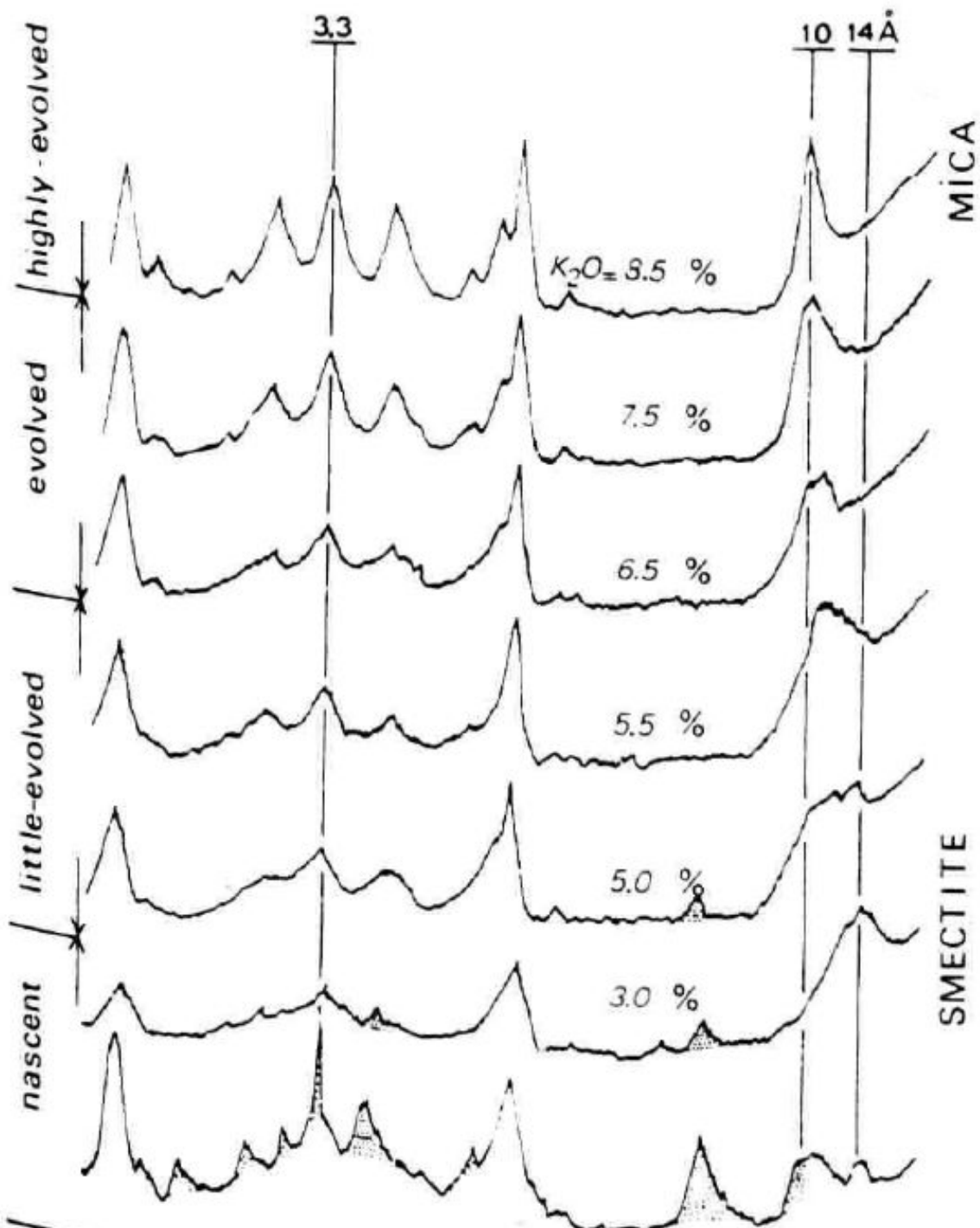


Fig. 6.3 The stability fields of iron minerals plotted on (a) an Eh– pS^{2-} diagram for a pH of 7.4 (pS^{2-} is the negative log of the activity of the sulphide ion), and (b) an Eh– $\log P_{CO_2}$ diagram (P_{CO_2} is the partial pressure of CO_2). In the latter case, the value of pS^{2-} is assumed to be so high (i.e. the activity of sulphur is very low), that pyrite and pyrrhotite do not plot on this diagram.

Table 6.3 Average concentration of Fe, Mn, Cu, Co and Ni (in percentages) of shallow- and deep-water sediments and ferromanganese nodules from three sea-floor settings. From Glasby (1977)

| | Nearshore sediments | Deep-sea sediments, Atlantic | Seamount nodules | Abyssal nodules | Active ridge nodules |
|-------|---------------------|------------------------------|------------------|-----------------|----------------------|
| Fe | 4.83 | 5.74 | 15.81 | 17.27 | 19.15 |
| Mn | 0.0850 | 0.3980 | 14.62 | 16.78 | 15.51 |
| Cu | 0.0048 | 0.0115 | 0.058 | 0.37 | 0.08 |
| Co | 0.0013 | 0.0039 | 1.15 | 0.256 | 0.40 |
| Ni | 0.0055 | 0.0079 | 0.351 | 0.54 | 0.31 |
| Depth | | | 1900 m | 4500 m | 2900 m |

stages of glauconitization



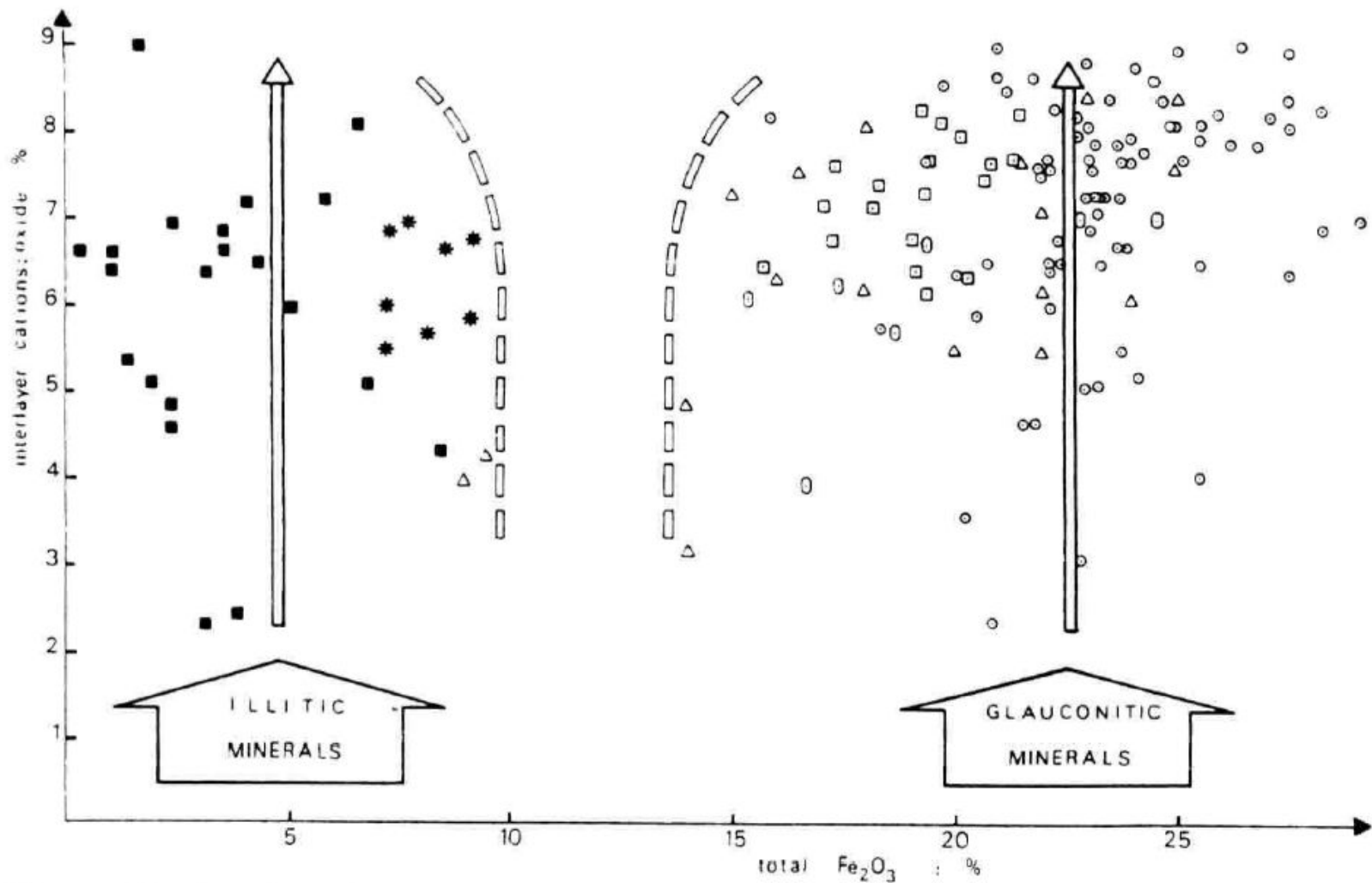
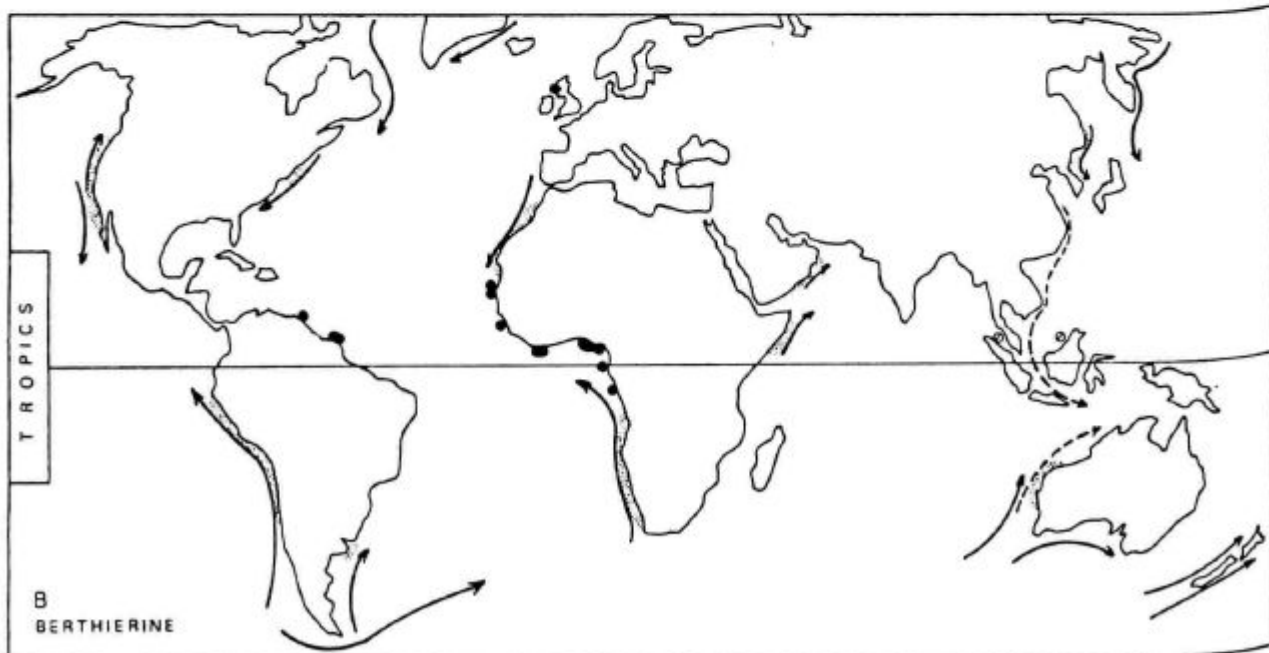
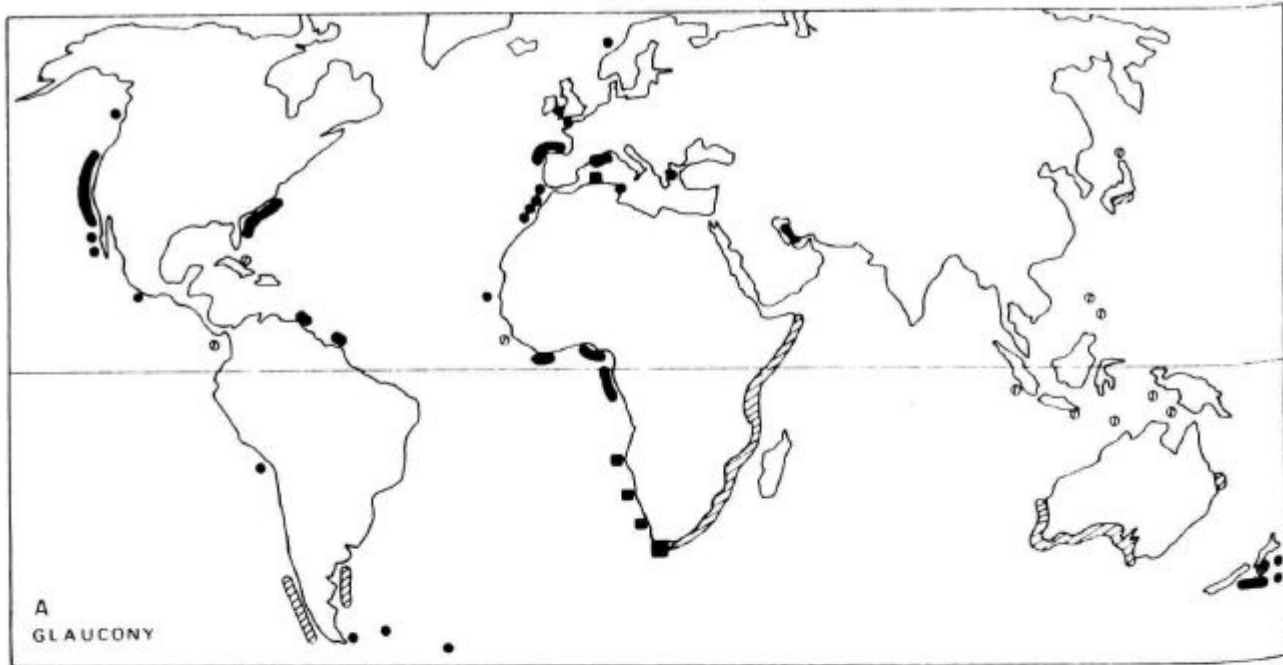


Fig. 8. Diagram showing the position of the illitic and the glauconitic mineral families with respect to their iron and interlayer cation content. Data from ○ Table 1, □ Cimbalnikova (1971a), ○ Parry & Reeves (1966), △ Hower (1961) —these samples appear to be mixtures of clay minerals of authigenic and of substrate origin—★ Kossovskaya & Drits (1970), ■ Hower & Mowatt (1966). Lack of values between about 10–15% Fe₂O₃ suggests absence of a mineralogical transition between illitic and glauconitic minerals. Arrows show evolution from a smectitic to a mica-type clay mineral within both families. Glaucony does not increase in iron content with increasing amounts of interlayer cations.



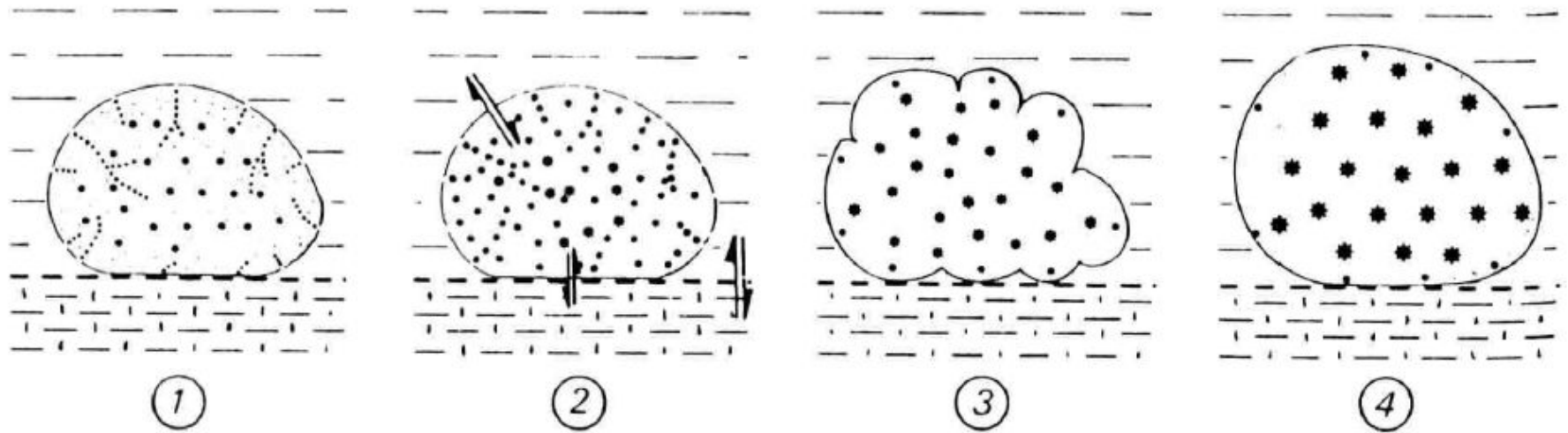


Fig. 12. Schematic representation of the evolution of a grain during glauconitization. Four stages from nascent (1) to highly-evolved (4) are selected from the continuum of changes observed in grains from the present shelf floor. Asterisks represent growth of glauconitic minerals. For discussion, see text.

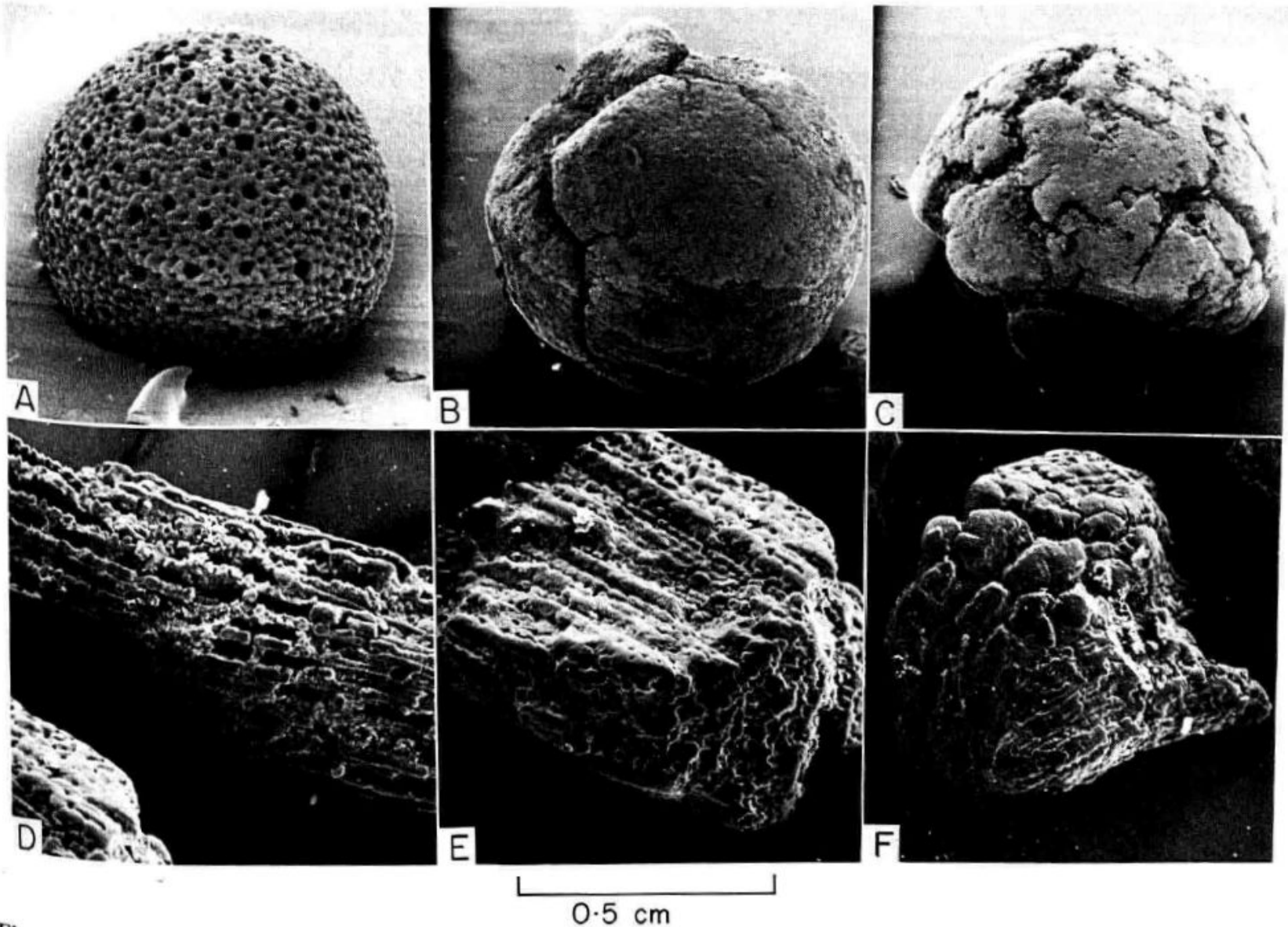


Fig. 15. SEM photomicrographs of *Orbulina* tests (A, B, C) and echinoderm fragments (D, E, F) showing progressive deformation during glauconitization. (A) *Orbulina* with pale green interior; (B) green mould with development of cracks; (C) dark green mould with large cracks leading eventually to splitting. Sequence (D) to (F) shows loss of original texture of echinoderm stereom during replacement by authigenic glauconitic crystals and development of a typical cracked grain.

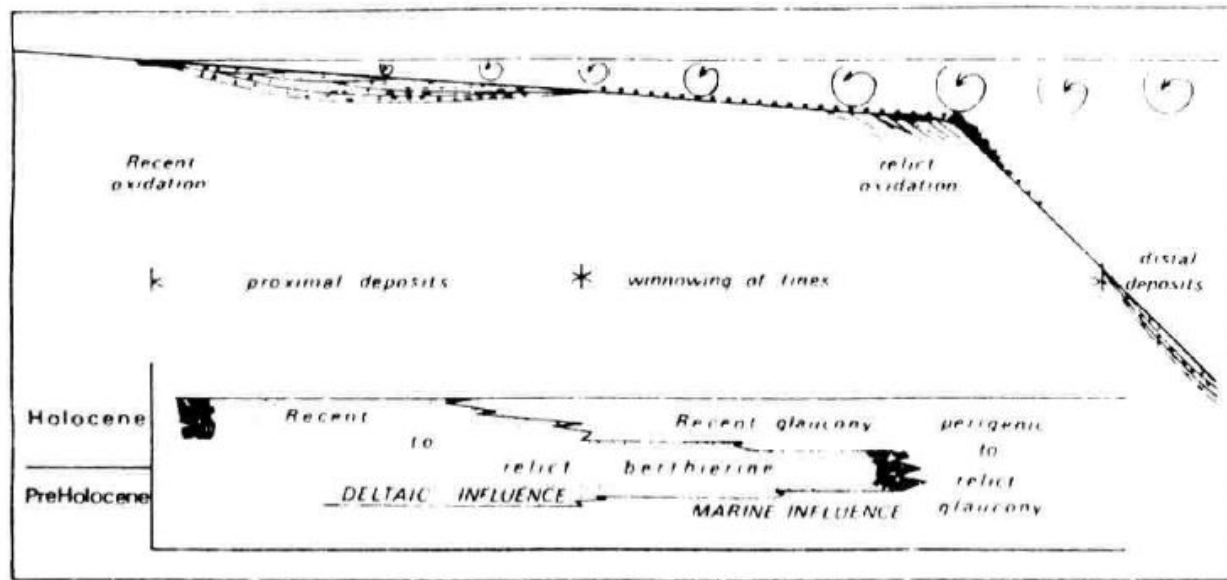


Fig. 18. Schematic diagram showing the environments of formation of glaucony and berthierine as a function of detrital influx and energy levels on a passive continental margin. Cross-section below shows facies relationships of glaucony and berthierine as a result of the Holocene transgression.

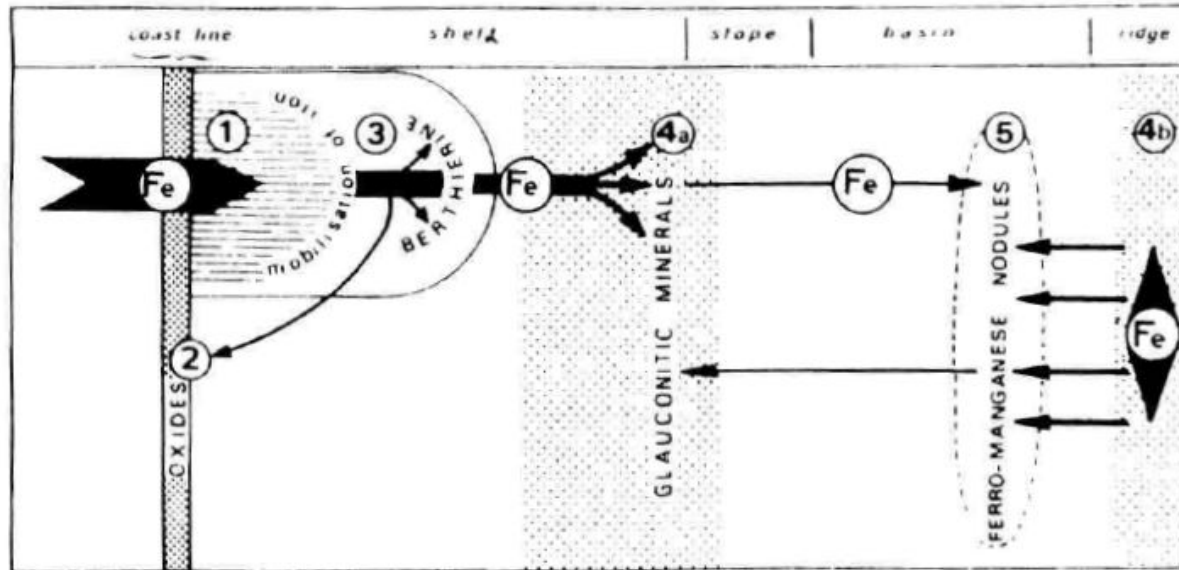


Fig. 19. Position of green sheet silicates in the geochemical path of iron in the sea. Zone 1, accumulation of detrital iron; zone 2, chemical precipitation of iron and oxidation of detrital iron minerals; zone 3, authigenic growth of berthierine; zones 4a, b, authigenic growth of glauconitic minerals; zone 5, growth of ferromanganese nodules. Modified from Odin (1975b).

| FACIES | TEXTURE | AUTHIGENIC MINERAL | | INHERITED | ENVIRONMENT |
|------------------|-----------------|-----------------------------------------------------------------------------------|-----------------------------------------------------------------------------------------------------------|----------------------------------------------|----------------------------------------------------------------------------------------------------------------------------------------------|
| | | (001) | K ₂ O | | |
| GLAUCONY | GRANULAR green | highly-evolved ----- evolved ----- little-evolved ----- nascent | 10Å glauconitic mica ----- -8% ----- -6% ----- 14Å glauconitic smectite ----- -4% | absent ----- ----- ----- present | non depositional 10 ⁵ - 10 ⁶ years ----- ----- non depositional 10 ³ - 10 ⁴ years |
| | FILM green | TOT glauconitic minerals | various minerals | break in sedimentation | |
| BERTHIERINE | GRANULAR green | 7.2Å berthierine | often present various minerals | deltaic influence | |
| ZEOLITE FACIES | VESICULAR green | TOT celadonite | volcanic | volcanic | |
| CHLORITIZED MICA | FLAKY green | 14Å chlorite | biotite | continental | |
| UNCERTAIN ORIGIN | DIFFUSE green | often undeterminable | often clay minerals | variable | |

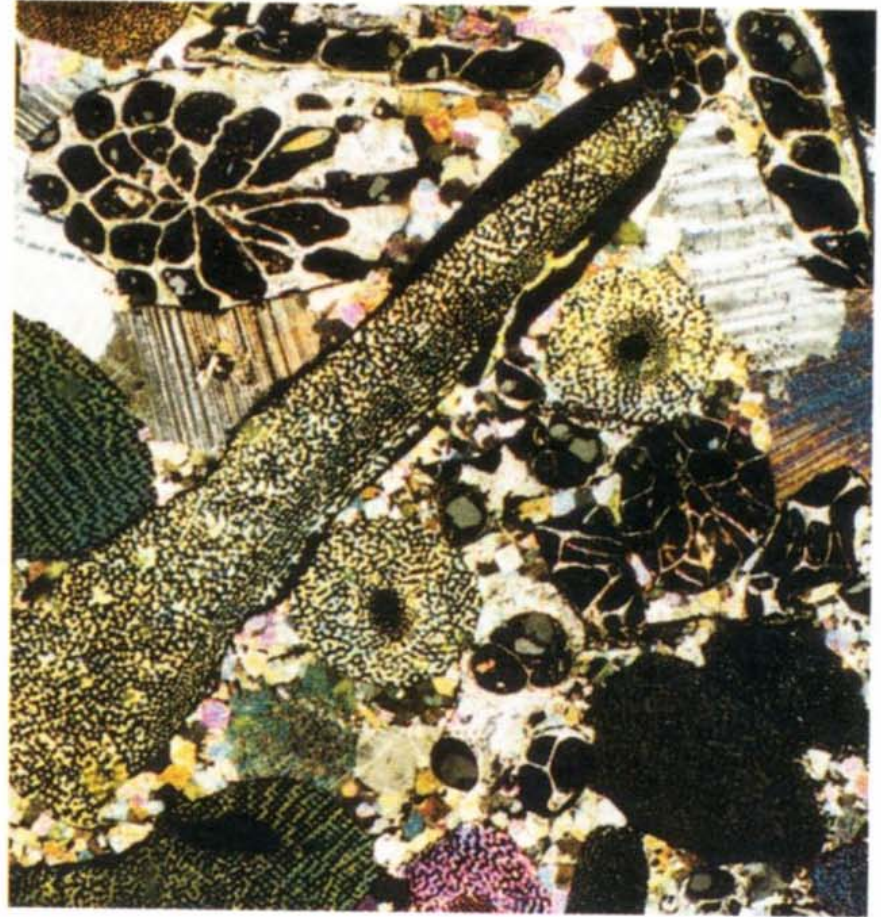
open marine

Fig. 20. Genetic classification of glaucony and related facies.

hematite ironstone



(c)

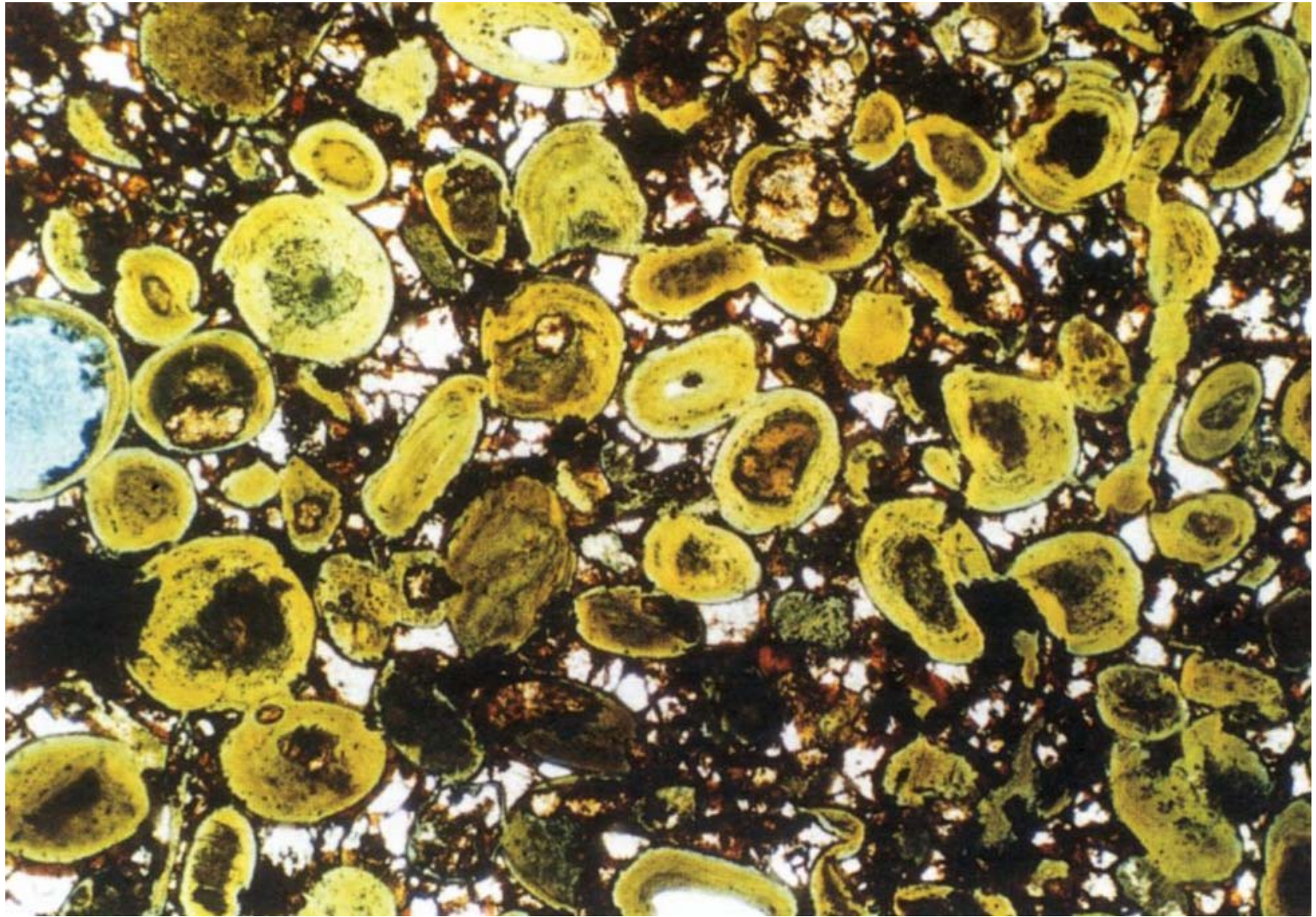


(d)

Crinoids, Bryozoans



chamosite ironstone
ooids



berthierine, chamosite, siderite, goethite

Phosphates

mineralogy (carbonate fluorapatite - CFA, frankolite, alophan)

distribution of present-day occurrences

genetic models of marine phosphates - upwelling, islands, atolls, sea mountains, guyots, epeiric seas

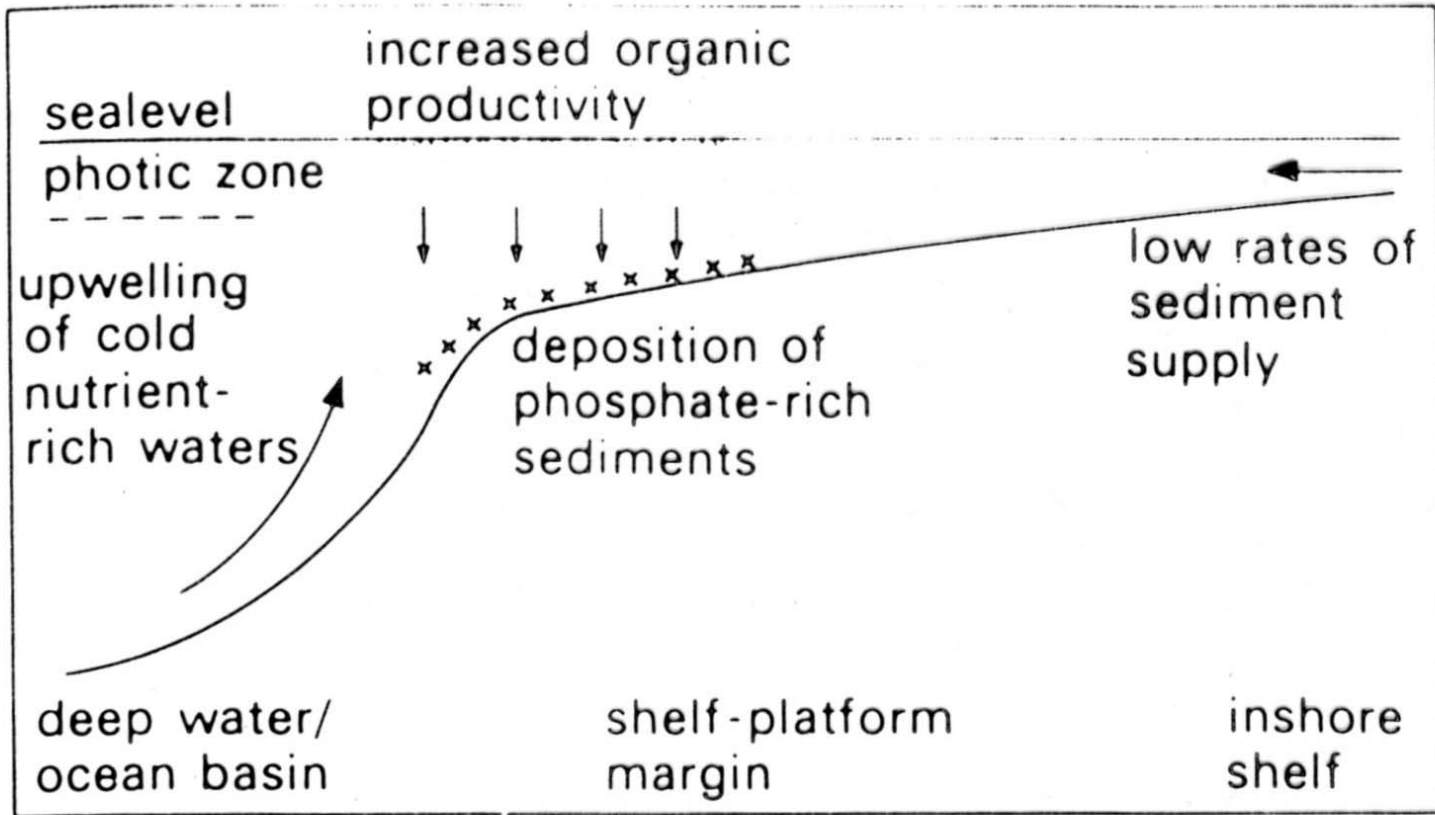


Fig. 7.2 Model for formation of marine phosphorites.

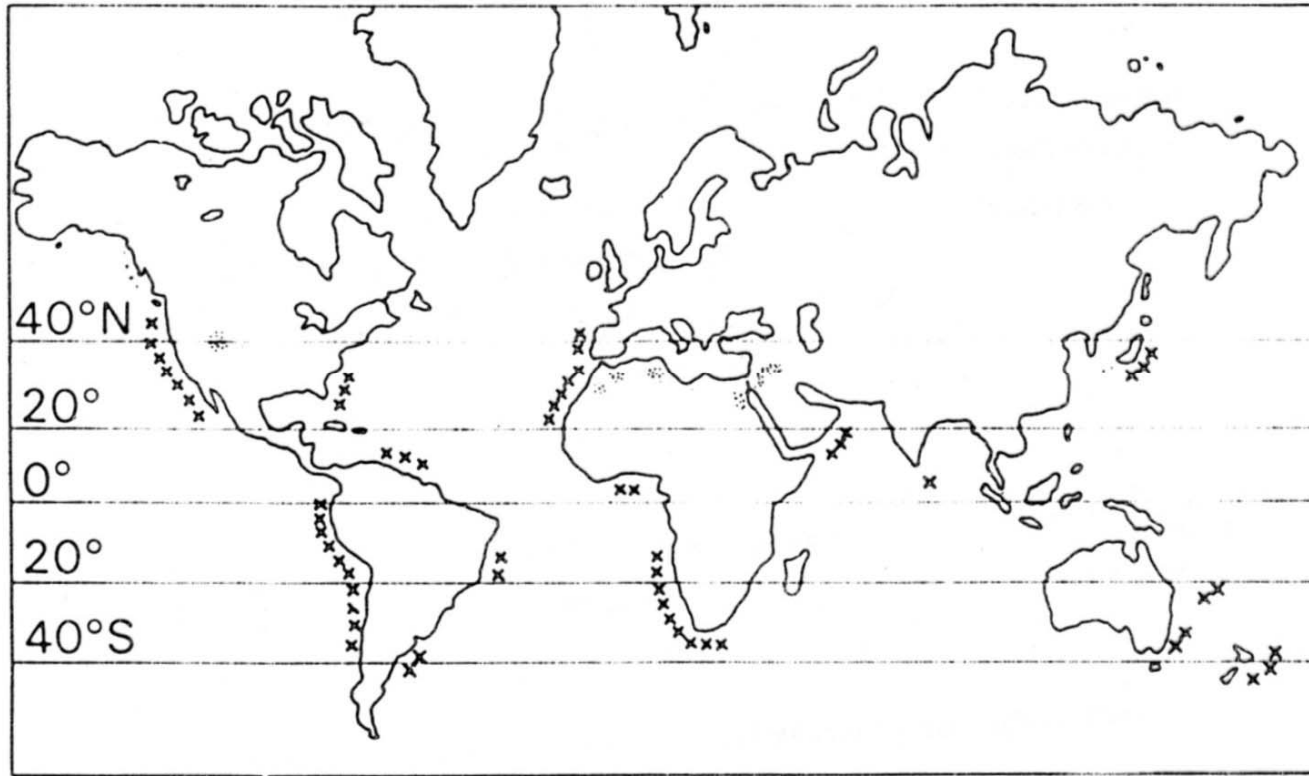
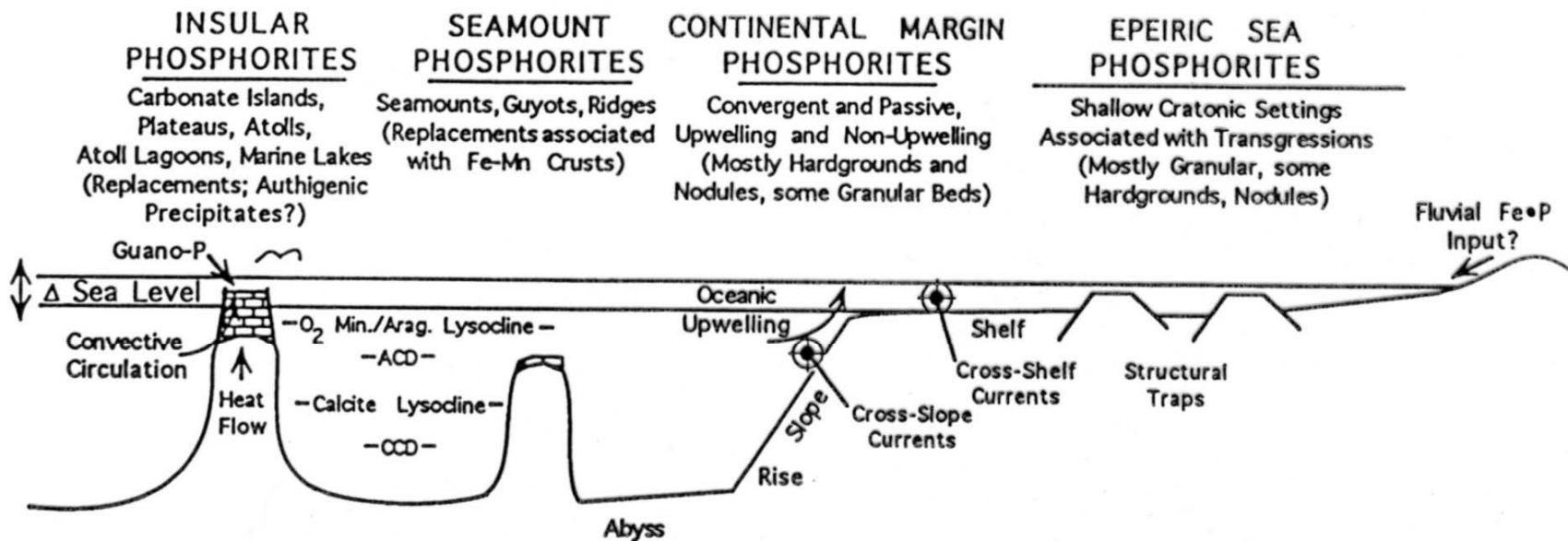


Fig. 7.1 Distribution of marine phosphorites, although in many cases the deposits are not actually forming at the present time. Also shown are the locations of the Permian Phosphoria Formation of northwestern USA and the Cretaceous–Tertiary phosphorites of the Middle East–North Africa.



EXAMPLES:

Modern
Palau Is.
Clipperton Atoll (?)

Modern
Pacific Seamounts?
(no data)

Modern
Peru-Chile, Namibia,
W. India, Baja California,
E. Australia

Modern
Absent

Ancient
South Pacific:
Naru, Banaba, Kita
Daito Jima, Makatea,
Line Islands

Ancient
Pacific Seamounts
Queensland Plateau

Ancient
Monterey Fm.,
Phosphoria Fm.(?),
SE USA

Ancient
See Figure 8

Indian Ocean:
Aldabra and
Christmas Is.

Fig. 1. Tectonic and oceanographic settings of marine phosphorites as derived from studies of the modern and ancient record.

1. *F-phosphates*: small nodules, peloids or laminae of friable, light colored CFA. These were called collophane mudstones by Burnett et al. (1980). Consistency varies from very friable and unconsolidated to more compact, though even the latter can be scratched with a fingernail. Presumably, F-phosphates age or mature to eventually become D-phosphates.
2. *D-phosphates*: well lithified, often dark and dense nodules, gravels and hardgrounds of CFA.
3. *P-phosphates*: phosphoritic sands dominated by structureless and coated (microbanded) phosphatic grains, with some admixtures of fish bones and teeth.

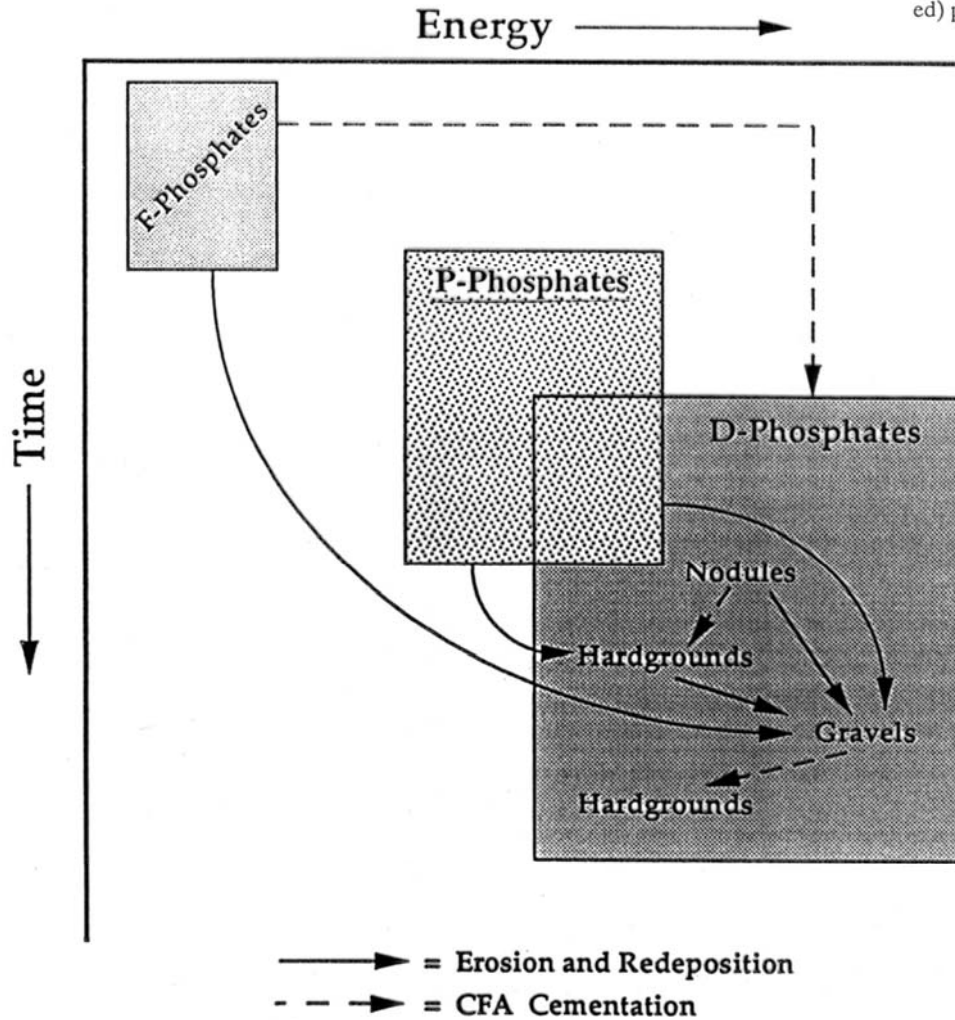
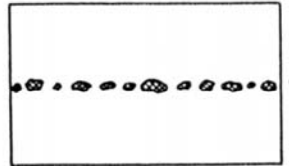


Fig. 2. Schematic portrayal of energy and time relationships for the formation and evolution of F-, P-, and D-phosphates. Shown also are the transitions among the three kinds of phosphorites that result from reworking and carbonate fluorapatite cementation on or near the sea floor. Modified from Garrison & Kastner 1990.

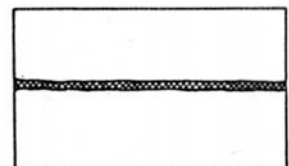
Stratification in phosphatic sediments as a function of time and energy

Stratification

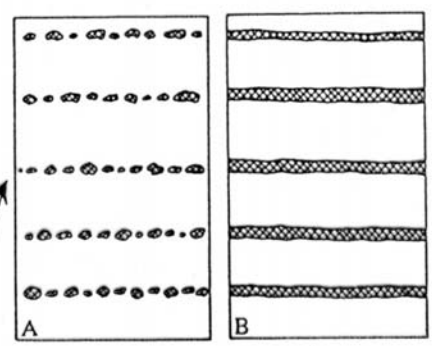
Phosphogenesis



In-situ phosphatic diaclasts

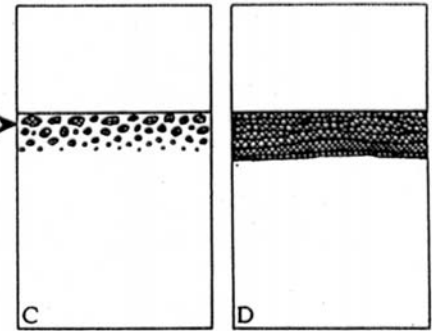


In-situ phosphatic lamina



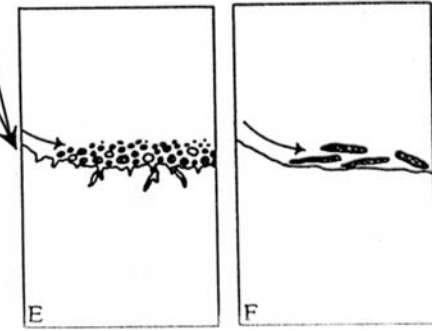
Accumulation rates > Erosion rates

"PRISTINE"



Accumulation rates \cong Erosion rates

"CONDENSED"



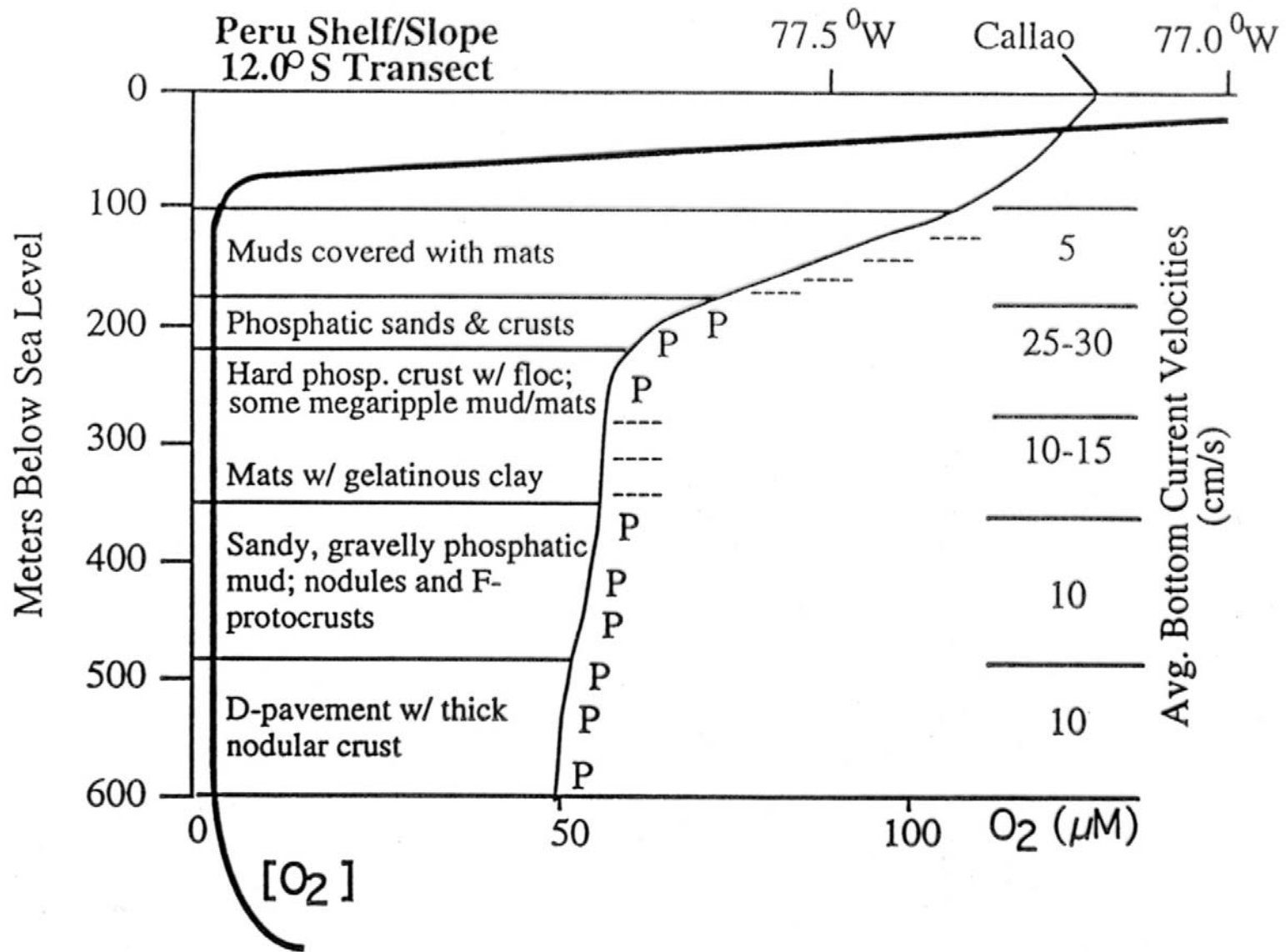
Accumulation rates < Erosion rates

"ALLOCHTHONOUS"

1. *Pristine*: phosphates which lack any signs of reworking.
2. *Condensed*: phosphatic laminae and particles which have concentrated by winnowing processes or bioturbation.
3. *Allochthonous*: phosphatic particles that have been entrained by and redeposited from turbulent and/or gravity-driven flows.

HYBRIDS

Fig. 3. Genetic classification of stratification types in phosphorites. From Föllmi et al. 1991, reprinted with permission of Springer-Verlag.



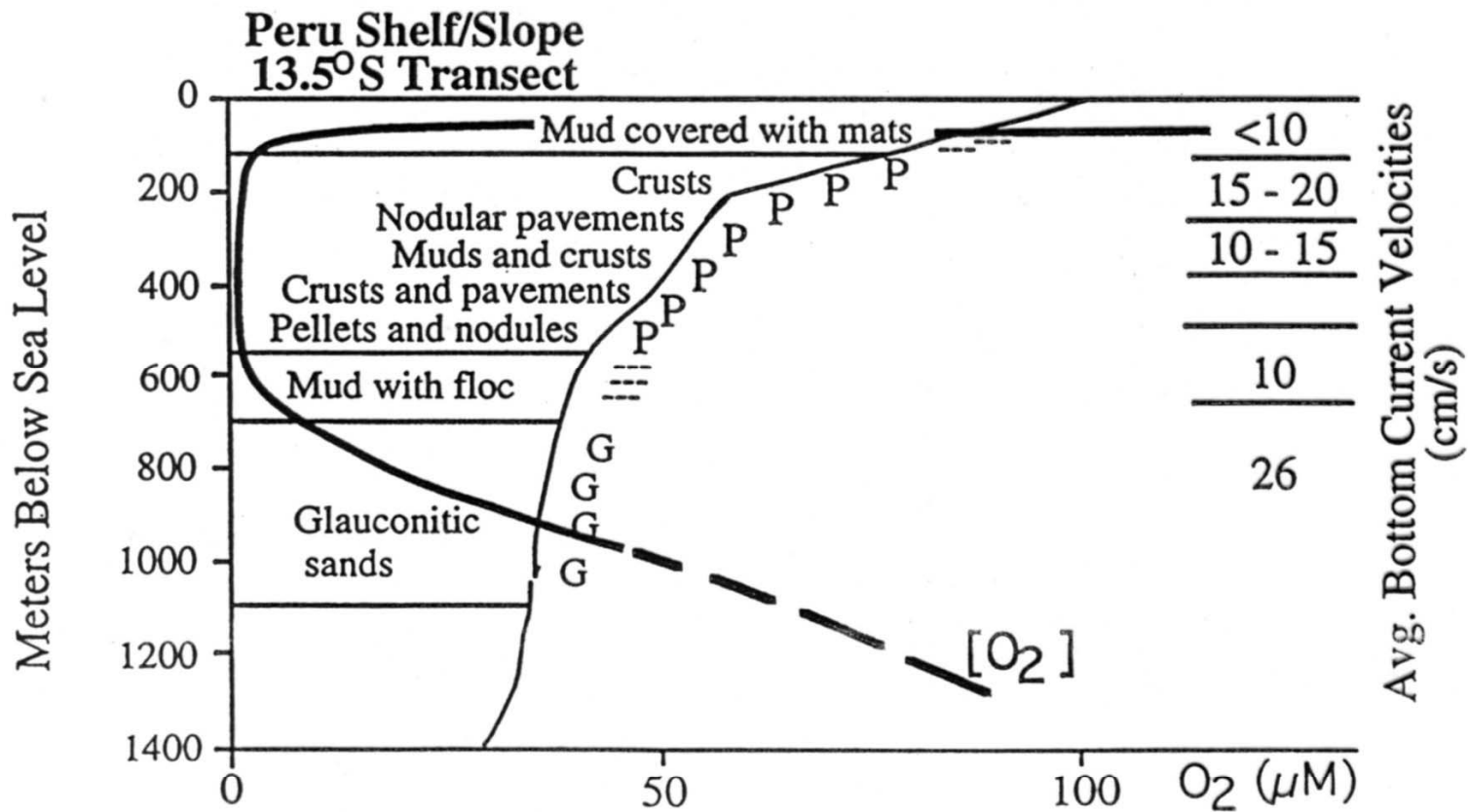


Fig. 5. Sediment and phosphorite distribution together with measured bottom current velocities (cm/s) and dissolved oxygen concentrations (μM) on the outer Peru shelf and upper slope at 12°S (top) and 13.5°S (bottom) (results from R/V *Seward Johnson*, 1992 cruise; unpublished). "P" represents distribution of phosphorite. Nodular hardground pavements and phosphatic sands occur in association with highest current velocities. Friable (F-phosphate) CFA-protocrusts occur between about 350 and 500 m. Glaucanitic sands occur along the base of the oxygen minimum zone between 700 m and 1100 m at 13.5°S . Bacterial mats are sulfide-oxidizing *Thioploca* sp. After Glenn et al. 1994.

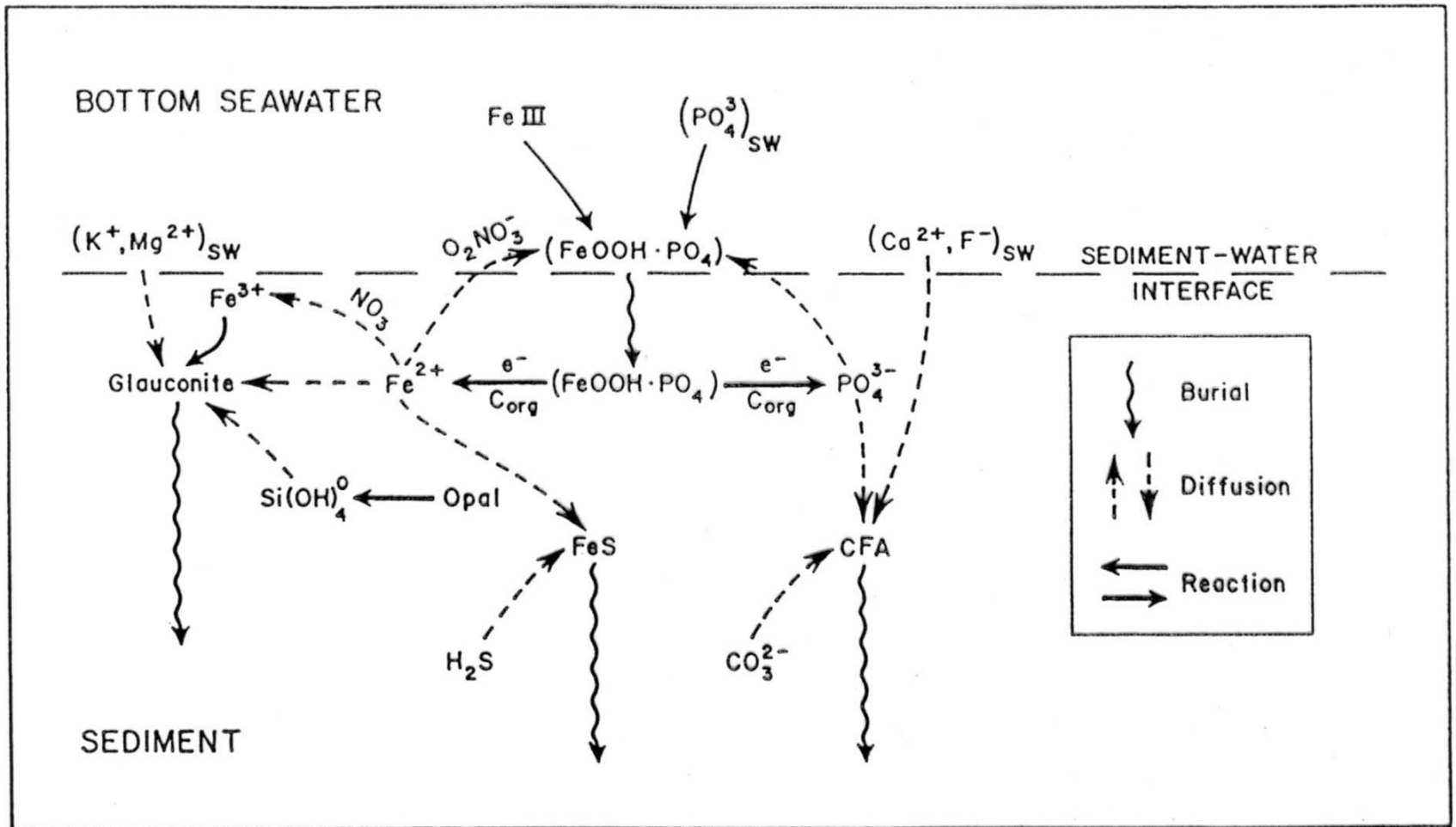


Fig. 6. Schematic diagram of iron redox-P cycle as postulated for Peru Margin sediments by Froelich et al. (1988). Iron hydroxyoxides sorb phosphate from bottom water and from upward diffusing pore water phosphate. Once reduced below the sediment-water interface these compounds release the sorbed phosphate to pore waters which is then precipitated. The reduced iron (Fe^{2+}) fluxes back to the more oxidizing environment of the bottom waters, where it may again sorb phosphate, or is precipitated in the sediments as a component of pyrite or glauconite. A somewhat similar mechanism has also been proposed for the modern sediments of the east Australian margin (see text). Reprinted with permission of Elsevier Science.

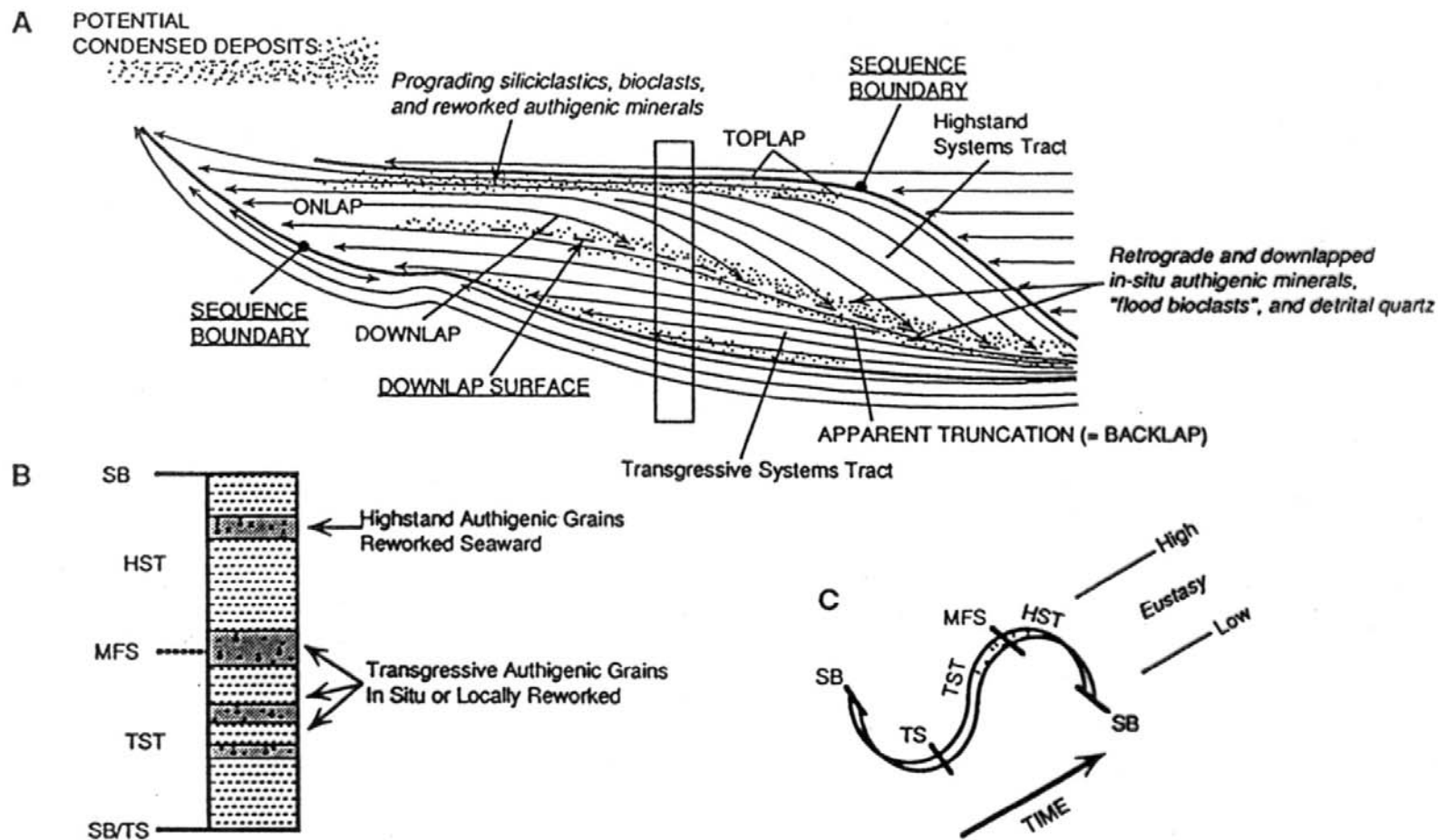
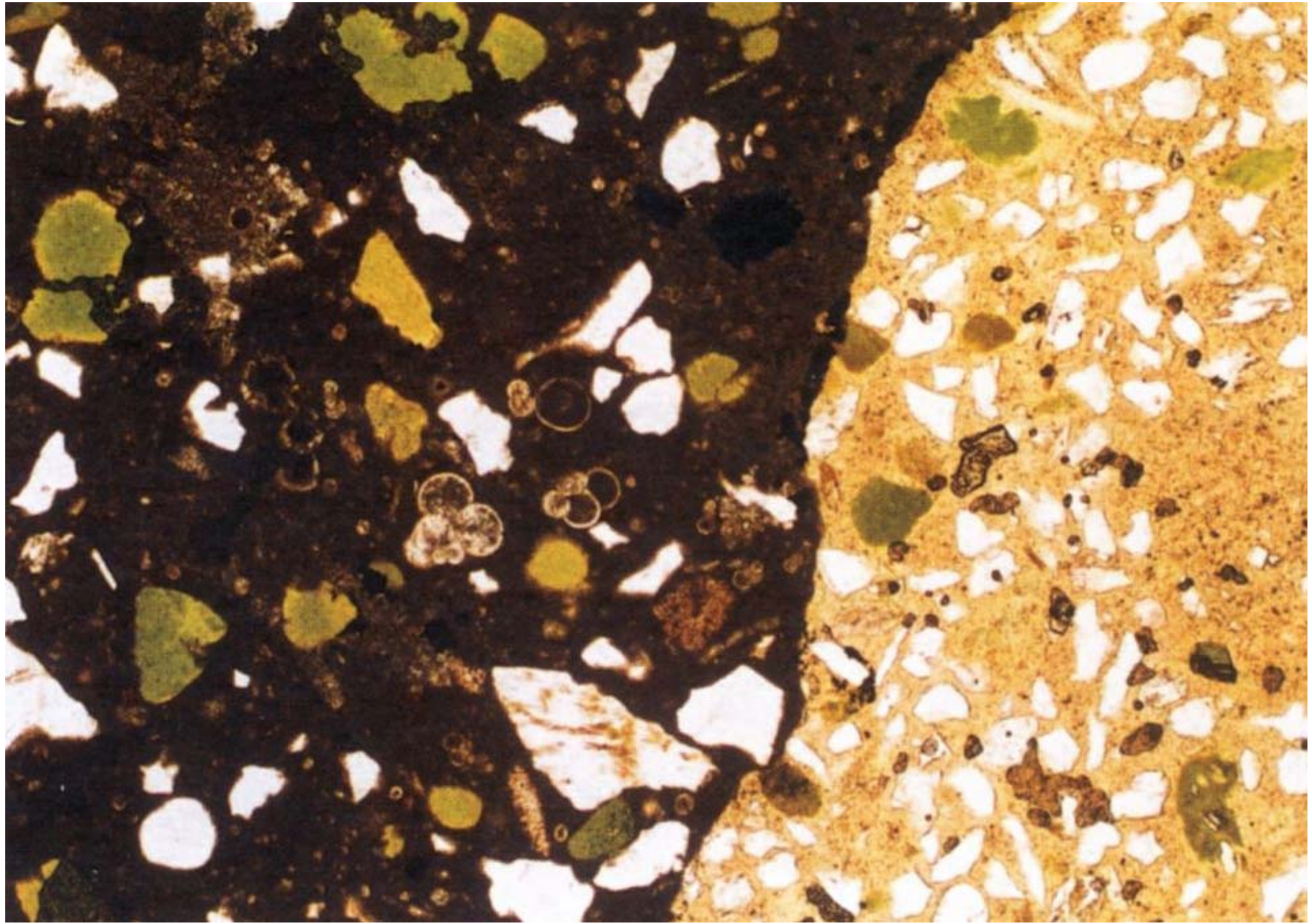
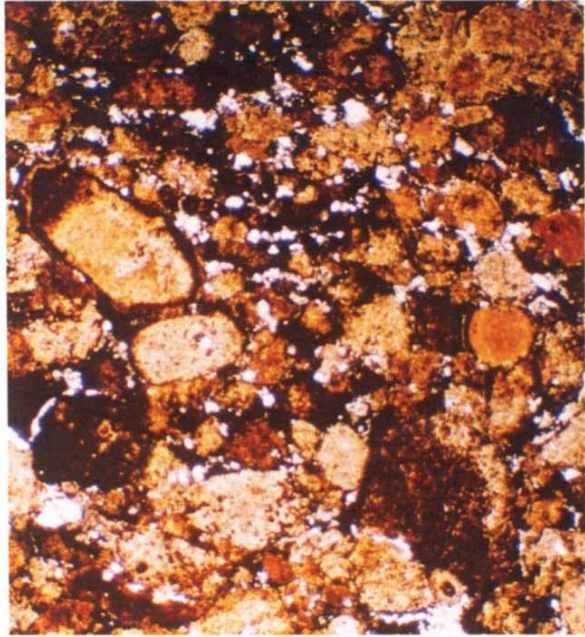


Fig. 10. Potential relationships between sequence stratigraphy, condensed sections and phosphorites. (A) Possible positions of sequence condensation within an idealized depositional sequence (stipples), (after Kidwell 1991). (B) Schematic illustration of the placement of non-reworked pristine authigenic phosphorite (and/or glauconite) and reworked phosphorite (and/or glauconite). Pristine phosphates may form within transgressive systems tracts and at the maximum flooding surface, whereas later phases are reworked seaward within highstand systems tracts. (C) The timing of systems tracts development with respect to one cycle of sea level change. LST = lowstand systems tract, TST = transgressive systems tract, HST = highstand systems tract, TS = transgressive surface, MFS = maximum flooding surface, SB = sequence boundary. Dots on the sea level curve represent locations of maximum phosphorite emplacement. After Glenn & Kronen 1993.



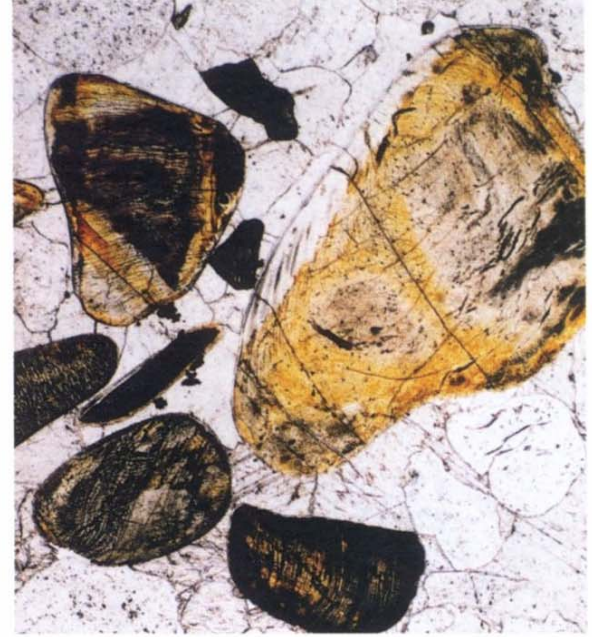
glaukony, phosphate



(c)



(d)



(e)

Reading:

M.E.Tucker: Sedimentary petrology. 3rd ed. Blackwell, 2001.

H. Blatt (1992): Sedimentary Petrology. Freeman & Co., New York.

G.S.Odin and A.Matter (1981): De glauconiarum origine. Sedimentology, 28, 611-641.

C.R.Glenn and 15 others (1994): Phosphorus and phosphorites: Sedimentology and environments of formation. Eclogae Geol. Helv., 87, 3, 747-788.